Recent Atom Probe Studies at IMR : a Comprehensive Review(APFIM/FIM)

著者	Hono Kazuhiro, Sakurai Toshio
journal or publication title	Science reports of the Research Institutes, Tohoku University. Ser. A, Physics, chemistry and metallurgy
volume	44
number	2
page range	223-240
year	1997-03-31
URL	http://doi.org/10.50974/00043823

Sci. Rep. RITU A44 (1997) pp. 223-240
No. 2, March 1997

Recent Atom Probe Studies at IMR - a Comprehensive Review*

Kazuhiro Hono[a] and Toshio Sakurai[b]
[a]*National Research Institute for Metals, 1-2-1 Sengen, Tsukuba 305, Japan*[1]
[b]*Institute for Materials Research, Tohoku University, Sendai 980-77, Japan*

(Received January 21, 1997)

This paper reviews our recent atom probe research activities conducted at Institute for Materials Research (IMR), Tohoku University, during a period of 1990 to date. The atom probe research started at IMR when the authors constructed an energy compensated time-of-flight atom probe in 1990. Since then, this instrument has been employed for various metallurgical problems, providing better understandings to mechanisms of microstructural evolution in various metallic materials. Notable achievements are studies of precipitation processes in aluminum alloys, nanocrystallization processes of amorphous alloys, microstructural characterizations of magnetic thin films and various other metallic materials. A new instrument equipped with a reflectron type time-of-flight atom probe and a position sensitive atom probe (PoSAP) was constructed in 1994. This instrument allowed three dimensional visualizations of atom distributions in alloys with an atomic resolution. PoSAP has been employed to characterize microstructures in Cr-Fe and Co-Cr(-Ta) magnetic alloys.

Keywords: atom probe, field ion microscope, FIM, APFIM, amorphous, nanocrystal, microstructure, phase transformation, precipitation

1. Introduction

Atom probe field ion microscopy is a unique microstructural characterization technique, which is capable of identifying individual atoms by time-of-flight mass spectrometry [1]. Using a field ion microscope, one can observe individual atoms which are protruding on the surface of the specimen. By selecting a small region using an aperture called "probe hole", it is possible to collect atoms only from the selected area. Atoms are evaporated from the surface by the field evaporation phenomena, and thus, it is possible to collect atoms in the depth direction of the selected area. The data chain of the collected atoms can be converted to a one dimensional depth profile of the specimen. Since atoms are ionized from the surface regularly, it is possible to resolve atomic layers in the field evaporation process. Thus, APFIM can determine local chemical compositional changes in less than a nanometer lateral resolution and an atomic layer depth resolution. This feature makes it possible to determine the chemical composition of nanoscale precipitate particles embedded in the matrix phase accurately, which is difficult with the conventional analytical instruments such as transmission electron microscope (TEM).

More recently, a new type of atom probe was developed by Cerezo et al. [2] by adopting a position sensitive detector in the time-of-flight atom probe, by which it is possible to determine both the mass and the position of individual atoms. This instrument is called a position sensitive atom probe (PoSAP), and it can map elemental distributions with a subnanometer resolution. The elemental maps can be extended to the depth direction by ionizing atoms from the surface of the specimen, by which atom distribution can be visualized in a three dimensional real space. Thus, this type of atom probe is generally called a three dimensional atom probe (3DAP). This technique provides additional information regarding the morphology of nanoscale microstructures in alloys compared to the conventional atom probe, and it has been demonstrated that this technique can reveal some critical problems in microstructures in alloys.

In this article, we review our atom probe research activities which were conducted at IMR during a period of 1990 to date. These include studies on solute clustering and precipitation in aluminum alloys, nanocrystallization of amorphous alloys, characterization of magnetic thin films, giant magnetoresistance and microstructures in granular alloys, studies of intermetallics, and phase transformation in steels.

2. Instruments and specimen preparation methods

Two types of atom probe field ion microscopes (APFIM) have been implemented for various applications. One is a Poschenreider type energy compensated atom probe, whose details are described elsewhere [3]. One of the notable feature of this instrument is its ability to cooling specimens to 20 K, by which stable imaging of aluminum alloys became possible. In earlier days, FIM observation and atom probe analysis of aluminum alloys were not common, while other major industrial materials such as steels were extensively studied. This was mainly due to low evaporation field of aluminum, which makes observation of FIM images difficult. By cooling down specimen temperature lower than 20 K, evaporation field of aluminum becomes as high as ionization fields of Ne and He, by which stable observations of Ne and He ion images become possible. In FIM, such temperature was readily achieved, because there is no need of a specimen tilting mechanism. In fact, using a dedicated FIM, good quality images were obtained by Abe et al. [4], Wada et al. [5], and Hirano and Hono [6]. In an atom probe, however, a specimen tilting mechanism has to be incorporated in the

* IMR, Report No. 2087

[1] Formerly (1990-1995), research associate at IMR, Tohoku Univeristy.

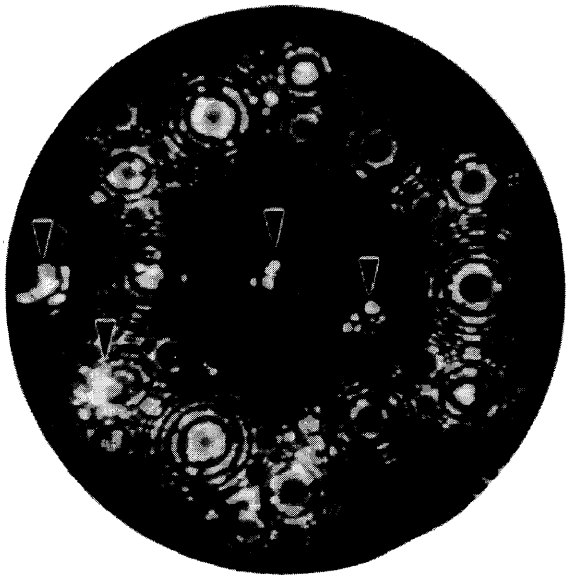

Fig. 1 He ion image of Al-6at.%Ag alloy aged at 130°C for 60 h.

FIM, and achieving 20 K is not trivial. Figure 1 shows He ion image of Al-6at.%Ag alloy aged at 130 °C for 60 h. This image demonstrates that good quality of FIM image of aluminum alloys can be achieved even with atom probe if the specimen stage is carefully designed.

Following the successful implementation of the first atom probe, a different type of atom probe instrument was implemented in 1994 [7]. The appearance of the instrument is shown in Fig. 2. As shown in the schematic drawing, this instrument is a combination of reflectron type energy compensated atom probe and a position sensitive atom probe (PoSAP). A reflectron energy compensator has a economical merit over the Poschenreider energy compensator, but Einzel lens has to be installed as the reflectron does not have focusing ability of ions. By rotating the specimen from the position for FIM observation and conventional atom probe analysis, PoSAP detector (KINDBRISK PDA60) can be used for three dimensional atom probe analysis. These atom probe are fully computer controlled, and once atom probe analysis is started after proper alignment, unattended operation is possible.

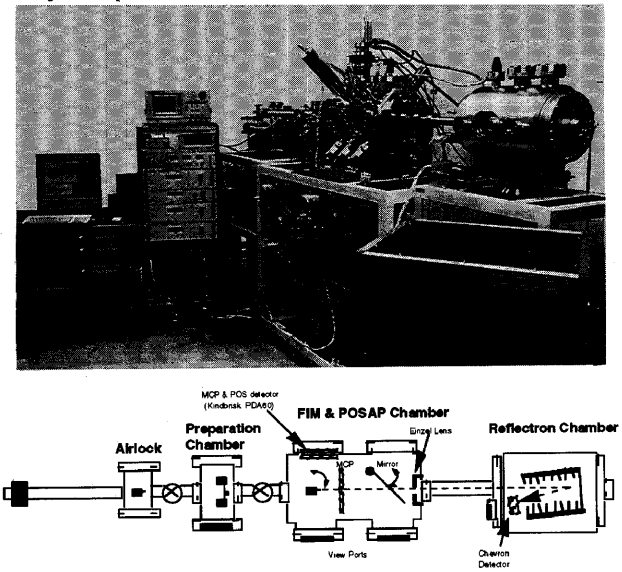

Fig. 2 An appearance and schematic drawing of the reflectron based atom probe with a PoSAP implemented at IMR.

One serious drawback of the atom probe technique is the specimen shape. The specimens has to be a sharp needle shape tip, whose diameter is ~100 nm. Most of bulk metallic specimen can be routinely prepared to sharp tips by electropolishing small square rods cut out from bulk specimens. Wire form specimens are readily prepared to a sharp tip by electropolishing. In addition to such standard metallic materials, there is a strong demand to prepare specimens from melt-spun ribbons for studying amorphous specimens and from thin films for studying metallic thin film microstructures. In order to prepare specimens from melt-spun ribbons, we have used a combination of mechanical polishing and micro-electropolishing. In this method, a short piece of ribbon typical 20 μm thick and 3 - 5 mm wide were embedded in acrylic resin plates. These were mechanically ground edge-on until a square cross sections was obtained [8]. These square rods were held on a nickel wire loop either by clamping with nickel tubing or by gluing with silver paste, and then micro-electropolished under an optical microscope [9]. For thin film specimens prepared by the sputter-deposition technique, we have applied the photolithography method and the microelectro polishing technique [10], and this made it possible to study magnetic thin films for recording media applications as well as nanocrystalline soft magnetic materials for recording head applications.

3. Solute clustering and precipitation in aluminum alloys

Most of wrought aluminum alloys are strengthened by precipitation hardening of solute elements, and it is known that trace addition of additional elements drastically changes kinetics and precipitation products in many age hardenable alloys. Precipitation in commercial aluminum alloys usually starts from formation of metastable coherent precipitates called G.P. zones and these evolve to more stable phases as aging goes on. This is because G.P. zones have less interfacial energy than the stable phases with completely different crystal structure and thus nucleation barrier is significantly less than those of stable phases. Typical sizes of G.P. zones are in the order of tens of nanometers, and chemical characterization of these zones cannot be easily done by other techniques. In addition, it has been suggested that some solute clustering occur prior to precipitation of G.P. zones, which modify kinetics of precipitation in may aluminum alloys. While G.P.zones are readily observed by modern TEM, observation of solute clusters is not possible with TEM. Atom probe can detect single atoms, and solute clustering in dilute alloys can be clearly detected.

Small additions (~0.1 at.%) of Ag and Mg are known to cause a complete change to precipitation processes that normally occur in aged Al-Cu and Al-Cu-Li alloys [11-14]. In Al-Cu alloy, combined addition of trace amount of Ag and Mg leads to precipitation of a new plate-like precipitate designated Ω on the $\{111\}_\alpha$ planes, in addition to the common precipitates in Al-Cu binary alloys on the {001} planes as shown in Fig. 3. The thinness of the Ω plates is attributed to the fact that they are coherent with the matrix along the $\{111\}_\alpha$ planes whereas there is a misfit of approximately 9% around the edges [12]. While T_1 phase precipitate heterogeneously at grain boundaries in Al-Cu-Li alloy, trace addition of Ag and Mg leads to uniform

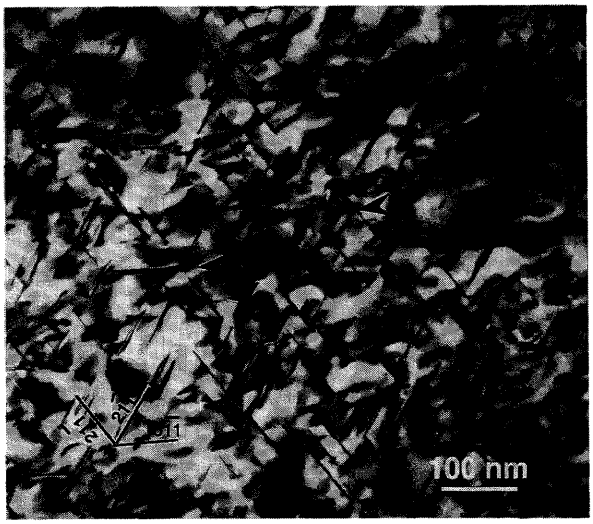

Fig. 3 TEM bright field image of Al-1.7Cu-0.3Mg-0.2Ag alloy aged at 190 °C for 8h. z~[011]. Some of θ' phases are arrowed.

distribution of T_1 on the $\{111\}_\alpha$ planes. These observations stimulated researches on mechanisms how trace addition of Ag and Mg completely modify the precipitation process in these alloys.

Atom probe studies by Sano et al. [15] found that both θ' and Ω phases have the same chemical composition (Al_2Cu) and thus Ω is the modified form of θ precipitate in compositional point of view. It was also shown that Mg and Ag are segregated at the Ω/α interfaces. Figure 4 shows an integrated concentration depth profile obtained in the normal direction to a $[111]_\Omega$ plate, and this convincingly shows that Ag and Mg are strongly segregated at α/Ω interfaces [16, 17]. This result suggests that segregation of Ag and Mg somehow modify the misfit between α/θ, which is usually too high to allow coherent precipitation with the $\{111\}_\alpha$ habit plane. If Cu is replaced with Ag and Al is replaced with Mg, θ phase can have good matching with the $\{111\}_\alpha$, and this might lead precipitation of θ at the $\{111\}_\alpha$ planes with a slightly modified form as Ω. Evidence for segregation of Ag and Mg were later confirmed using high resolution EDX using a field emission TEM by Howe et al. [18].

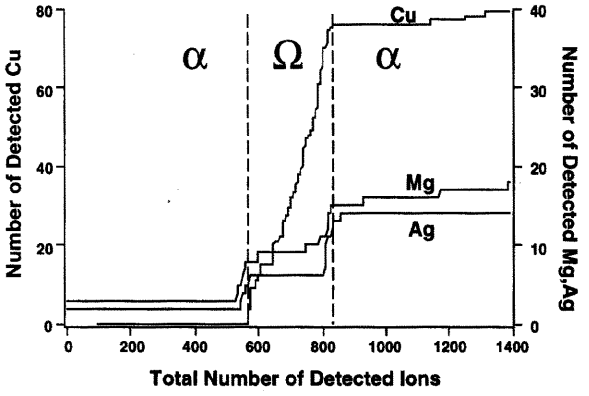

Fig. 4 An integrated concentration depth profile across the α/Ω/α interfaces obtained from Al-1.7Cu-0.3Mg-0.2Ag alloy aged for 2 h at 190 °C. Strong segregation of Mg and Ag at α/Ω interfaces is apparent.

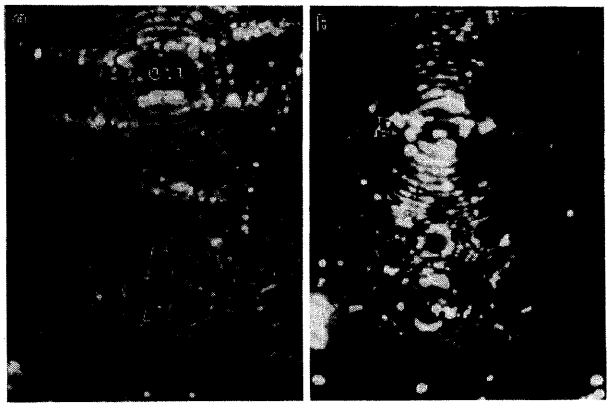

Fig. 5 He FIM images of (a) G. P. zone and (b) θ" observed in Al-1.7Cu-0.3Mg-0.2Ag alloy.

In addition to the Ω phase, G.P. zones, θ" and θ' phases which are commonly observed in Al-Cu alloys precipitate on the {001} planes in aged Al-1.7Cu-0.3Mg-0.2Ag alloys. Figures 5 (a) and (b) show FIM images of G.P. zones and θ", respectively. Brightly imaging lines correspond to atomic rows of Cu atoms and it is clearly seen that G.P. zones are of single layer platelet, while θ" contain two atomic layers of Cu separated by a few layers of Al atomic layers. Atom probe analysis showed that no Ag and Mg were incorporated into θ" phase at the stage that Ω phase coexist, while G.P. zones contained Ag and Mg atoms before Ω phase precipitated at aging temperature below 160 °C.

Atom probe studies were further extended to the pre-precipitation stages of this alloy [19,20]. In the as-quenched state, individual clusters of Mg, Cu and Ag have been detected. However, these clusters have no correlation each other. By aging only for 15 sec, Mg and Ag show clear

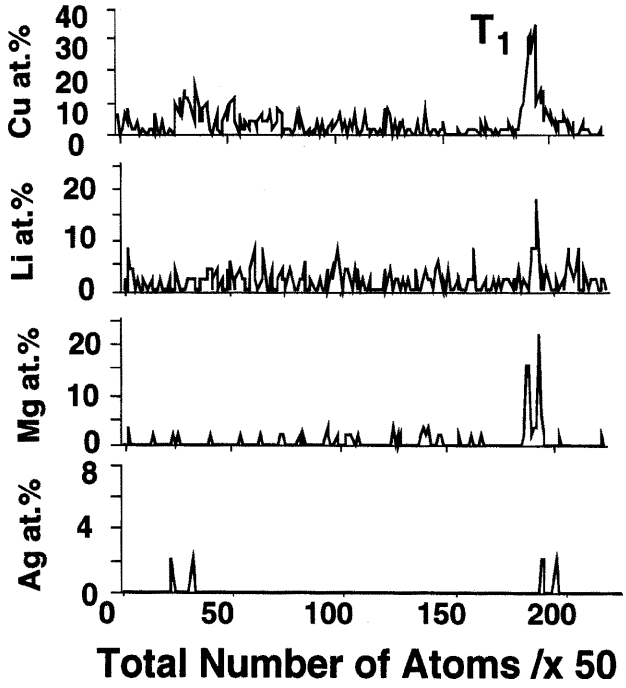

Fig. 6 Atom probe concentration depth profile of a Weldalite 049 alloy (Al-5Li-2.25Cu-0.4Mg-0.1Ag-0.04Zr) aged at 200 °C for 2 h. Ag and Mg atoms are enriched in the T_1 phase.

correlation and they form co-clusters of Ag and Mg. Similar tendency was observed in the Al-1.7Cu-0.3Mg ternary alloys [20], i.e. co-clusters of Mg and Cu were detected after 30 sec aging at 180 °C. By TEM observation, it was found that ternary alloy contains a number of dislocation loops, while Ag containing quaternary alloy contains little dislocation loops in the as-quenched state. This observation suggests that Ag atoms trap vacancies during quenching. By short time aging, Ag and Mg form co-clusters in the quaternary alloy, while Mg and Cu form co-clusters in the Al-Cu-Mg ternary alloy, suggesting that Mg and Ag has strong affinity. After 30 sec aging, Cu was found to be associated with the Ag and Mg, but at this state, TEM observation showed indication of small precipitates on the $\{111\}_\alpha$ planes. From these result, it has been concluded that Ag and Mg co-clusters act as nucleation sites for Ω, and no precursor phase something like Ω' are present, unlike previous report by Avis [21].

Trace addition of Ag and Mg cause uniform dispersion of T_1 phase in Al-Cu-Li-Mg-Ag alloys [13,14], while T_1 precipitate heterogeneously at grain boundaries in Al-Cu-Li alloys. While precipitate product is different from the case of Al-Cu-Mg-Ag alloys, uniform dispersion of thin plate-like precipitate on the {111} plane is very similar phenomena. From our results of the Al-Cu-Mg-Ag alloy, it is anticipated that Ag and Mg segregation might have close link with the uniform dispersion of the T_1 phase in the Al-Li-Cu-Mg-Ag (Weldalite) alloy. Figure 6 show atom probe analysis results of the Weldalite 049 alloy (Al-5Li-2.25Cu-0.4Mg-0.1Ag-0.04Zr) aged at 160 °C for 10 h [22-24]. From this concentration profile, incorporation of Ag and Mg to the T_1 phase is apparent. Both Mg and Ag appear to be incorporated into the T_1 phase. Since Li has very low evaporation field, evaporation rate become very fast when T_1 phase appear on the specimen surface, leading degradation of spatial resolution and quantitativeness of the data. However, the data clearly show that Ag and Mg are strongly associated with the T_1 phase and this must somehow assist uniform dispersion of the T_1 phase in grains.

Cluster formation in the precipitation stage was found to be common in many age hardenable aluminum alloys. In Al-Cu-Mg alloys having Cu:Mg ratios <1.5, it has been known that G.P.B zones form in the early stage, followed by heterogeneous precipitation of S phase (Al_2CuMg) [25]. A unique feature of this alloy system its fast age hardening response in the early stage as shown in Fig. 7 [26, 27]. Within 60 sec of aging at 150 °C, the hardness increase sharply and then reach a stage of slow age hardening response. After this hardness plateau, the hardness curve show the second stage. In early study by Polmear [28], the first stage was ascribed to formation of G.P.B. zones and the third stage was to formation of S'. Ringer et al. [26, 27] studied precipitation process of Al-1.1Cu-1.7Mg alloy and found that no precipitate contrast was observed by TEM in Stage I of the age hardening curve. Atom probe analysis results of this stage, however, indicated that co-clusters of Mg and Cu were present, while independent clusters of Cu and Mg were present in the as-quenched alloy. From this result, the 1st stage of the age hardening response in this alloy is concluded to be due to solute cluster formation, and they designated this phenomena as "cluster hardening effect". However, no sufficient explanation is given how solute cluster formation can contribute to such remarkable hardening. G.P.B zones and S phase are found to form in Stage III in Fig. 7 [27]. Ringer et al. [26] concluded that S' is in fact the same as the S phase. Solute clustering in early stages were reported in other aluminum alloy systems, such as Al-Cu-Sn [29] and Al-Mg-Si [30] alloys.

Phase decomposition in Al-Li alloy is of great controversy as to whether ordering precede to phase decomposition or *vice versa*. Atom probe analysis of Al-7.8at.%Li alloy convincingly showed that in the as-quenched stage, the alloy is phase decomposed to α and δ', and it has been suggested that this system is not appropriate to test possible occurrence of the congruent ordering reaction prior to the decomposition, as the kinetics of the decomposition is too fast to suppress and separating these two stages are unrealistic using any microscopy techniques [31,32].

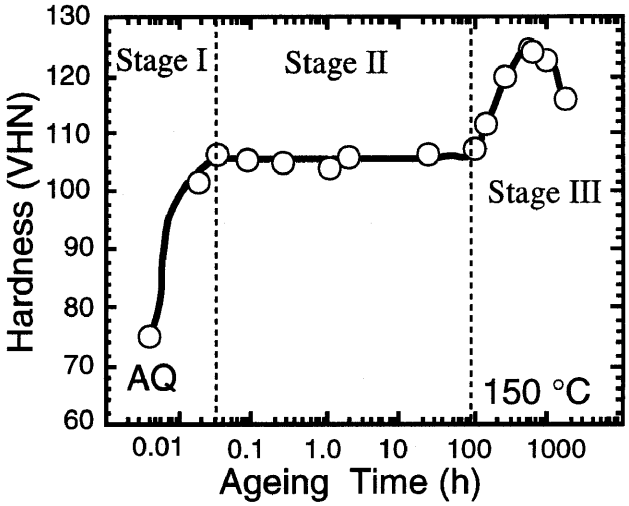

Fig. 7 Hardness vs. aging time curve of the Al-1.1Cu-1.7Mg alloy aged at 150 °C [26].

4. Nanocrystallization of amorphous alloys

There is an increasing interest in synthesizing nanostructured materials anticipating appearance of new properties by reducing the physical dimensions of materials such as sizes of crystal grains, various phase domains and precipitate particles. Recent examples of nanocrystalline soft [33-37] and hard magnets [38] and nanocrystalline ultra-high strength aluminum alloys [39-43] indicate that the synthesis

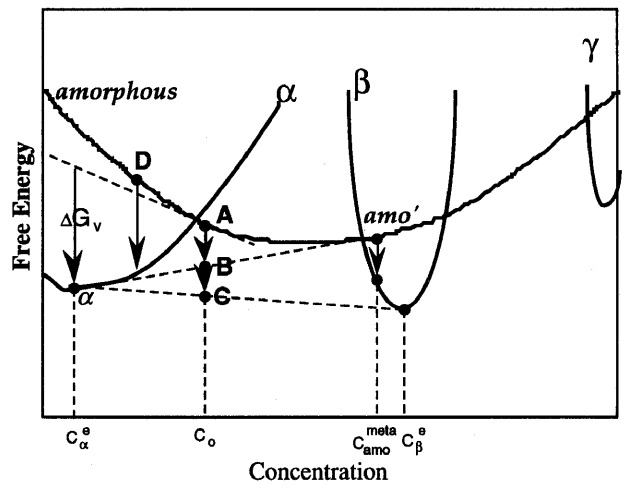

Fig. 8 Schematic free-energy concentration diagram of a model amorphous binary alloy. Primary crystallization is expected at C_0, where primary α-phase precipitate in an amorphous matrix.

of nanocrystalline alloys can lead to the development of new materials with unconventional properties.

A typical nanocrystalline structure occurs when the amorphous alloy is crystallized by primary crystallization. A schematic free-energy and concentration diagram of a model amorphous alloy is shown in Fig. 8. When the amorphous phases with compositions D is annealed, crystallization will occur without any change in concentration. This type of crystallization is known as polymorphous crystallization [44] and the microstructure obtained by this process is in general composed of coarse crystal grains as the grain can grow *massively* without long range diffusion. In a later stage, the supersaturated α phase decomposes to achieve thermal equilibrium composed of α and β phases. On the other hand, when the amorphous phase with a composition A crystallizes, α phase precipitate from the matrix amorphous phase. The concentration of the nuclei will be determined so that the chemical driving force for nucleation (indicated as ΔG_v in Fig. 8) can be the maximum. Since the concentration of the nuclei is significantly different from that of the matrix amorphous phase, long range diffusion has to be involved in this crystallization process. This is called primary crystallization, and the microstructure obtained by this process is in general very fine. If large homogeneous nucleation rate or a high number density of nucleation sites is provided and the subsequent grain growth rate is effectively reduced, nanocrystalline microstructure forms by the primary crystallization process. When primary phase precipitate from an amorphous phase, the concentration of solute in the remaining amorphous phase increases and it may reach as high as that of the β phase. However, such microstructure is still in the metastable state composed of the α and amorphous phases (indicated by a tangent α-amo' in Fig. 8), and if this is further annealed, the equilibrium state will be achieved by the polymorphous crystallization of the residual amorphous phase (amo'). When intermetallic compound precipitate by the polymorphous crystallization, gross grains precipitate from the remaining amorphous phase. Hence, crystallization process in the amorphous alloys which form nanocrystalline structure will progress in two stages;

amorphous → α + amo' → α + β,

where α is the initial phase which precipitate from the amorphous matrix and β is a intermetallic compound of the solute and the solvent elements. In fact, isochronal differential scanning calorimetry (DSC) curves of these materials show two distinct peaks corresponding to each crystallization stage [34, 36, 39]. The nanocrystalline structure often appears after the first stage of the crystallization reaction. Needless to say, the actual amorphous alloys are not simple binary alloys, and more than one type of intermetallic phases are expected in the second stage. Hence, the crystallization process in the multicomponent amorphous alloy should be more complicated. In this section, we will show typical examples of directly measured atom probe concentration depth profiles of various amorphous alloys in the course of primary crystallization, and it will be seen that the above described process is in fact observed experimentally.

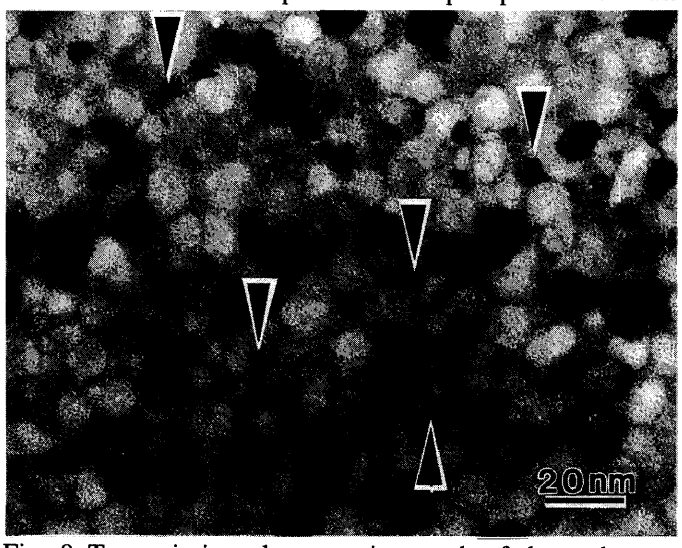

Fig. 9 Transmission electron micrograph of the melt-spun $Fe_{73.5}Si_{13.5}B_9Nb_3Cu_1$ alloy annealed at 823 K for 60 min. Two types of grains are recognized. The grains indicated by arrows were identified to be fcc Cu.

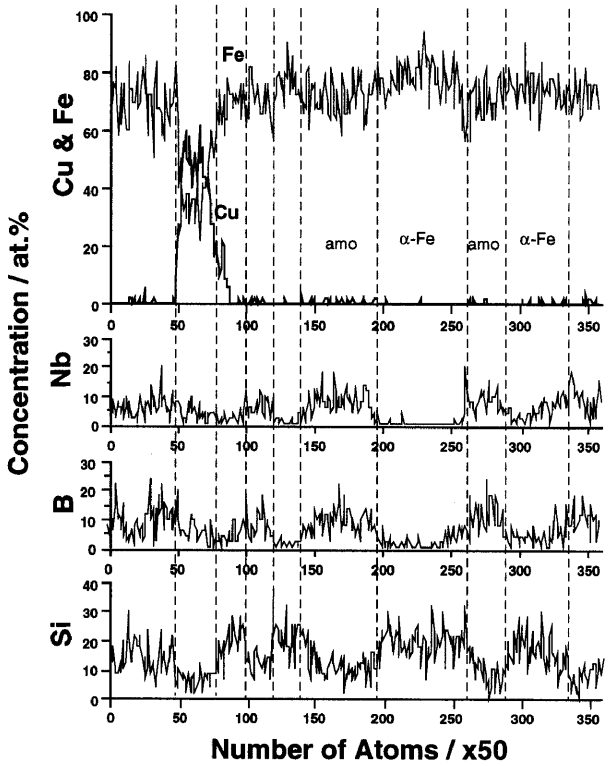

Fig. 10 Atom probe concentration depth profile of the melt-spun $Fe_{73.5}Si_{13.5}B_9Nb_3Cu_1$ alloy annealed at 823 K for 60 min.

4.1 Fe-Si-B-Nb-Cu

The most well-known and pioneering nanocrystalline material which makes good use of the primary crystallization process is Fe-13.5Si-9B-3Nb-1Cu alloy, which is commercially known as FINEMET [33,34]. This nanocrystalline alloy exhibits very high permeability and its origin is ascribed to the reduced magnetocrystalline anisotropy due to the random distribution of nanoscale grains [45,46]. Yoshizawa et al. [33, 34] investigated the crystallization process of various Fe-Si-B based amorphous alloys and found that the nanocrystalline structure was obtained by adding both Cu and Nb in Fe-Si-B based alloys. Figure 9 shows a typical electron micrograph of this alloy produced by the primary crystallization process. This consists of the nanocrystalline bcc phase with an average grain size of approximately 10 nm. In addition, smaller grains can be recognized as indicated by arrowheads. Since the combined addition of Nb and Cu is required for nanocrystallization, the role of Nb and Cu for nanocrystallization was of great research interest. For this

Fig. 11 Ne filed ion micrograph of melt-spun $Fe_{73.5}Si_{13.5}B_9Nb_3Cu_1$ amorphous alloy.

study, atom probe was found to be extremely effective technique [47-49].

Figure 10 shows atom probe concentration depth profiles of the $Fe_{73.5}Si_{13.5}B_9Nb_3Cu_1$ alloy with the optimum magnetic properties (annealed at 823 K for 60 min.). The presence of three types of phases are clearly identified. One is enriched with Si (~20-25 at.%) but contains little Nb, Cu and B. Complementary TEM observations suggested that this region was the crystallized bcc α-Fe phase containing Si. In addition to the α-Fe grains, a B and Nb enriched amorphous phase is present with little Cu content but containing some Si. In addition to these two phases, a Cu enriched particle is observed. This phase was significantly enriched in Cu (~60%) but still contains appreciable amounts of Nb, B and Si. Since the concentration of Fe is only about 30%, this phase is believed to be nonmagnetic. In fact, a separate nanobeam electron diffraction study in a transmission electron microscope (TEM) revealed that the Cu enriched particles were fcc Cu [49]. This phase appears as a grain having a diameter of approximately 5 nm as indicated by arrows in Fig. 9.

By analyzing the as-quenched specimen by TEM, FIM and atom probe, it was confirmed that the as-quenched alloy was a structurally and chemically uniform amorphous phase within the limitation of the spatial resolution of these techniques[2]. Figure 11 shows a typical field ion micrograph of the as-quenched specimen. Bright spots observed in the FIM image correspond to individual atoms protruding on the surface. If small crystal is present, regular arrangement of bright spots should be observed. In this image, however, no indication of presence of crystal structure is observed. Bright spots distribute randomly, indicating that the arrangement of

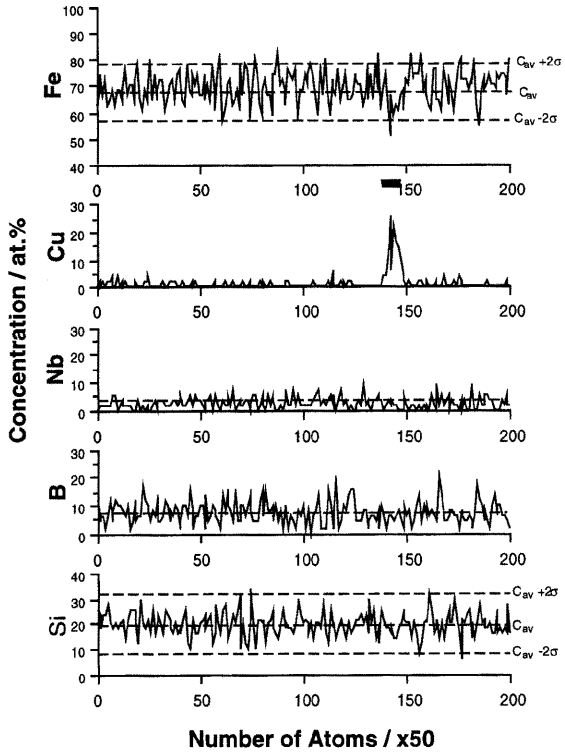

Fig. 12 Atom probe concentration depth profile of the melt-spun $Fe_{73.5}Si_{13.5}B_9Nb_3Cu_1$ alloy annealed at 450 K for 60 min. Separate TEM observations showed that this is still in the amorphous state. The broken lines show experimentally measured average concentration, C_{av}, and statistical errors expected from $C_{av}\pm\sigma$, where σ stands for the standard deviation.

atoms in the as-quenched specimen is entirely random[3]. When the as-quenched amorphous sample was annealed below the crystallization temperature, i.e. 523 K for 60 min., it was confirmed to remain still amorphous by TEM and FIM observations. However, atom probe concentration depth profiles showed that small Cu enriched clusters, a few nanometer in diameter, with at least 20 at.%Cu were present as shown in Fig. 12. This suggests that Cu clusters form in the very early stage of heat treatment even before the onset of the crystallization reaction.

Based on the atom probe analysis results and complimentary TEM observations, the nanostructure evolution by the primary crystallization process is summarized as Fig. 13. The Cu rich clusters form in the amorphous state before the onset of the crystallization. Similar conclusions were recently reported by EXAFS studies by two independent groups [50-52]. This cluster formation also causes a concentration fluctuation of Fe, since Cu substitutes for Fe. Thus, the density for the nuclei of the bcc

[2]Atom probe technique is not able to obtain information on short range ordering (SRO), because field evaporation of atoms from amorphous surface does not retain information of the nearest neighbor atoms.

[3]Since not all atoms contribute to bright spot formation, it will be difficult to recognize extremely small crystallites with only a few unit cell. This means that FIM images do not resolve topological short range ordering (TSRO). So it is not really productive to discuss the structue of amorphous alloys based on the FIM images. In this paper, if no indication of crystallites are observed with TEM, SADP and FIM, we call it as amorphous phase.

FeSi crystalline phase increases significantly. Once the α-Fe phase forms, Nb and B are excluded from the α-Fe and are enriched in the remaining amorphous phase because they are insoluble in the α-FeSi phase. As the annealing proceeds further, the size of α-Fe increases. At the same time, the Si content of this phase increases to ~25 at.% as Si tends to be partitioned to the α-Fe phase. Since the Nb and B enrichment in the amorphous phase stabilizes the remaining amorphous phase, grain growth of the α-Fe phase eventually stops. The Cu concentration in the Cu-rich clusters also increases as the crystallization progresses. The clusters grow to around 5 nm and the concentration of Cu increases to ~60 at.% or higher. This phase eventually becomes an fcc Cu particle.

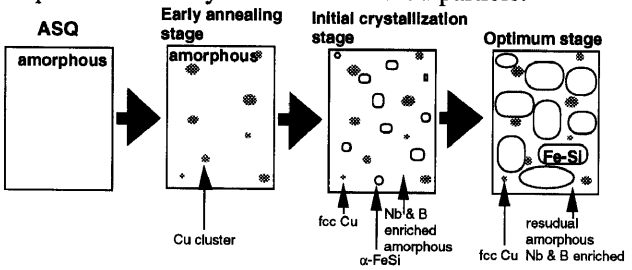

Fig. 13 A schematic illustration of the primary crystallization process of $Fe_{73.5}Si_{13.5}B_9Nb_3Cu_1$ alloy.

4.2 Fe-Ta-C

Fe-Ta-C nanocrystalline soft magnetic thin films, commercially known as Nanomax, are based on a similar principle as the above mentioned nanostructured soft magnetic material, but these films are fabricated by the sputtering process [35,53,54]. The as-deposited phase is amorphous and the nanocrystalline structure evolves by the subsequent heat treatment. Since Ta forms a thermally stable carbide, TaC, and this pin down the grain growth, thermal stability of this material is good enough to allow manufacturing process of metal-in-gap (MIG) head. The final microstructure is composed of nanocrystalline α-Fe and extremely fine TaC. The saturation magnetization obtained in this material is higher than that can be achieved in the Fe-Si-B-Nb-Cu alloy, because the α-Fe does not contain significant amount of solute elements. The Fe-Ta-C thin films form nanocrystalline structures by crystallization from the amorphous phase without any addition of nucleation enhancing elements such as Cu. Also, the isochronal DSC curve of Fe-Ta-C show only one exothermic peak [53], which is significantly different from the other nanocrystalline materials. Hence, the crystallization seems to progress without any distinguishable two stage processes.

Figure 14 (a - c) show Ne field ion images of Fe-Ta-C film with various heat treatments [55]. The distribution of bright spots in the field ion image of the as-deposited film (Fig 14 (a)) is random. This suggests that the as-deposited sample has an amorphous structure with homogeneous chemical composition. Note that two types of bright spots can be recognized. One appears sharp and smaller, the other appears diffuse and larger. We speculate that sharp and smaller spots correspond to Fe atoms. The diffuse and larger spots are thought to correspond to either C, Ta or Ta-C clusters based on the fact that the transition metal carbide in steels are reported to display diffuse and brighter contrast [56]. Figure 14 (b) shows a Ne ion image of the sample annealed at 673 K for 20 min. In earlier works [55], it was confirmed by TEM that the sample was completely amorphous phase after this

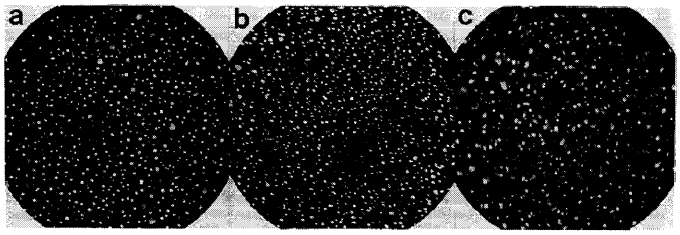

Fig. 14 Ne field ion images of Fe-7C-10Ta sputtered thin films (a) as-deposited, (b) annealed at 673 K for 20 min. and (c) 823 K for 20 min.

heat treatment. This FIM image also implies that the structure of this sample is still amorphous. However, notice that the distribution of the diffuse spots is significantly different from the as-deposited sample. The diffuse spots appear to be localized at various areas as indicated by arrowheads in Fig. 14 (b). The appearance of such contrast may be ascribed to the formation of C clusters or Ta-C pairs by annealing at 673 K before the crystallization is initiated. Figure 14 (c) shows a Ne field ion image of the sample annealed at 823 K for 20 min. Unlike previous FIM images, the diffuse and brighter spots form more distinct regions. These regions are believed to be C enriched region or TaC. On the other hand, the dimly imaging regions with the smaller bright spots are believed to be α-Fe grains. Note that the diffusely and brightly imaging regions look interconnected, surrounding the dimly imaging α-Fe grains. This suggests that C and Ta are being rejected from α-Fe grains.

Figure 15 (a-c) shows concentration depth profiles of Fe-Ta-C thin films with various heat treatment conditions. It appears that in the as-deposited alloy, carbon concentration fluctuations are larger than that expected for a homogeneous amorphous solid solution (errors expected from two standard deviations, 2σ, are indicated by dotted lines in Fig. 15 (a)). The maximum concentration of carbon reaches 30 at.%. Ta concentration fluctuations also appear, but they seem less significant compared to that of carbon. A statistical test of this concentration depth profile suggested that the distribution of carbon is not homogeneous. This result suggests that the fluctuation of carbon concentration might have been present in the as-deposited sample. Figure 15 (b) is a concentration depth profile of an amorphous specimen annealed at 673 K for 20 min. The fluctuation of the carbon concentration was enhanced compared to that of the as-deposited sample. The

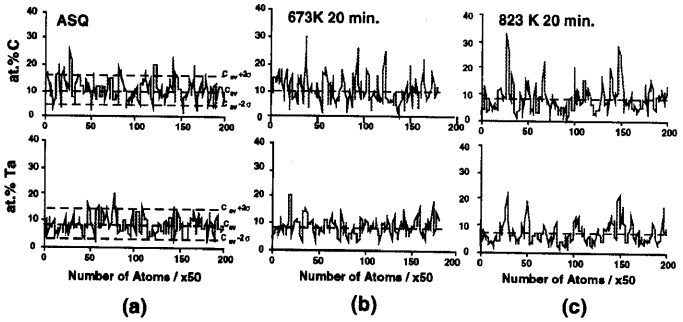

Fig. 15 Concentration depth profiles of Fe-7C-10Ta thin films (a) as-deposited, (b) annealed at 673 K for 20 min. and (c) 823 K for 20 min. The broken lines show experimentally measured average concentration, C_{av}, and statistical errors expected from $C_{av}\pm 2\sigma$, where s stands for the standard deviation.

highest concentration of carbon reached 30 at.%. Hence, the concentration fluctuations seem to be enhanced by heat treatment even below the crystallization temperature. Figure 15 (c) shows concentration depth profiles of carbon and Ta in the sample annealed at 823 K for 20 min. The carbon concentration peaks reached 40 at.%, which is close to that of TaC. The Ta concentration, however, appears to be lower than the expected value. The reason for this discrepancy is not clear at this moment. Between the carbon and Ta peaks, significant levels of dissolved carbon and Ta are detected inside grains. This means that the alloy did not yet reach thermal equilibrium. However, this figure clearly demonstrates that the phase separation progressed significantly in this stage.

These atom probe results suggest that fluctuations of carbon concentration may be present in the as-deposited amorphous phase. It was found that this compositional fluctuation was enhanced by the heat treatment even below the crystallization temperature as in the case of FeSiBNbCu amorphous alloy. In the case of Fe-Ta-C amorphous alloy, the high density of the nucleation sites of the crystalline phase may be explained by the presence of the compositional fluctuation of carbon in the early annealing stage. Pure iron is unstable as amorphous phase. If the carbon compositional fluctuation develops, the carbon depleted region will become unstable as the amorphous phase. Then such a region crystallizes to carbon supersaturated tetragonal iron. Since α-Fe has only a few atomic percent of solubility with Ta, Ta atoms must be rejected from such crystallized regions. Naturally, Ta would diffuse out of the crystallized regions into the amorphous phase, where the carbon concentration becomes higher. With longer annealing, TaC forms by nucleation from the carbon and Ta enriched amorphous regions. Since TaC can pin the grain boundaries of α-Fe, it works for retarding grain growth during further heat treatment. Since TaC is a thermally stable phase, this pinning effect will work even at a higher temperature.

4.3 Fe-Zr-B

4.3.1 Primary crystallization in Fe-Zr-B amorphous alloy

Fe-Zr-B alloys developed by Suzuki et al. [36, 37] exhibit high permeability with nanocrystalline structure. The crystallized microstructure consists of a large portion of nanocrystalline α-Fe particles embedded in a small fraction of the residual amorphous phase. The thermal analysis and x-ray diffraction results [37] showed that the crystallization of the amorphous Fe-Zr-B occurred through two distinct stages, i.e.,

amorphous→α-Fe+amorphous'→α-Fe+Fe_2Zr+Fe_3Zr.

The mechanism of nanocrystalline microstructural evolution in Fe-Zr-B seems to be different from that in Fe-Si-B-Nb-Cu alloys, because the former does not require addition of Cu, which has a large enthalpy of mixing with Fe, for nanocrystallization. Hence, it is expected that there is a large density of nucleation sites or that the rate of homogeneous nucleation is high in Fe-Zr-B alloy. One proposed mechanism to explain evolution of nanocrystalline structure in Fe-Zr-B amorphous alloy is spinodal decomposition which occurs prior to the crystallization reaction [57], but no convincing evidence for this mechanism has been presented.

Zhang et al. [58-61] made comprehensive atom probe studies on the nanocrystallization process of the Fe-Zr-B based amorphous alloys. By APFIM and TEM, the as-quenched Fe-7Zr-3B alloy was confirmed to be homogeneous supersaturated solid solution with the amorphous structure. In order to test the possibility of the proposed spinodal decomposition [57], the Fe-7Zr-3B amorphous alloy was annealed at 673 K for 60 min. and was observed by TEM and atom probe, but no noticeable difference was observed compared with those in the as-quenched specimen. Based on this result, they ruled out the possibility of the spinodal decomposition mechanism. In the HREM images, however, some regions that display a contrast which is similar to that of the medium range ordered (MRO) structure proposed by Hirotsu et al. [62, 63] was found. This feature was observed even in the as-quenched alloy, but after annealing at 673 K for 60 min., such MRO like contrast was observed more clearly. This indicates that very small MRO domains are developed during annealing below the crystallization temperature and that these may act as nucleation sites for primary crystallites.

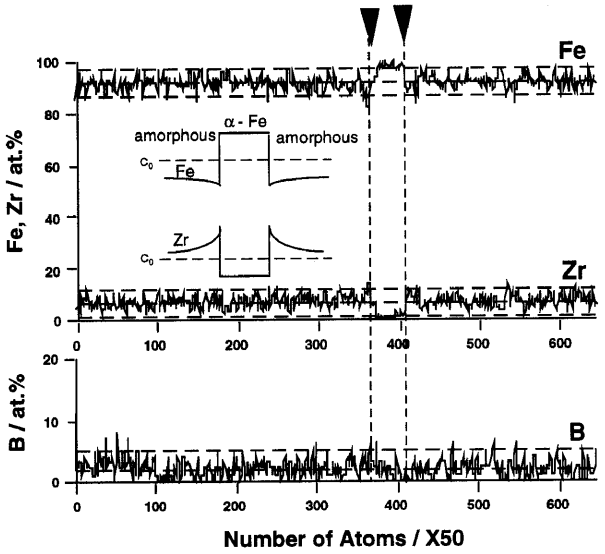

Fig. 16 Atom probe concentration depth profiles of Fe-7Zr-3B annealed at 723 K for 60 min.

Figure 16 shows atom probe concentration depth profiles of Fe, Zr and B at the nucleation and growth stage of a primary crystal. This specimen was annealed at 723 K for 60 min., and a separate TEM observation indicated that the

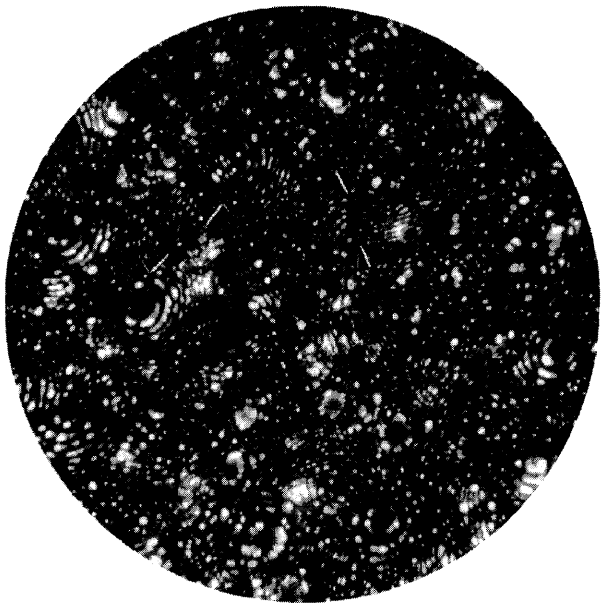

Fig. 17 Ne FIM image of Fe-7Zr-3B alloy annealed at 923 K for 5 min.

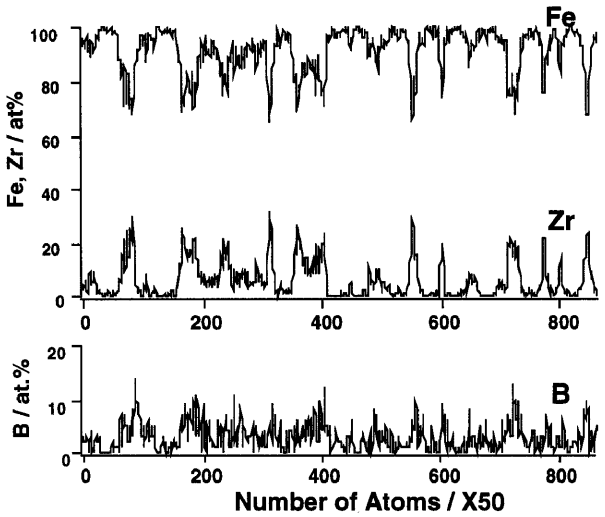

Fig. 18 Atom probe concentration depth profiles of Fe-7Zr-3B annealed at 923 K for 5 min.

majority of the phase was still amorphous [58]. Note that Zr atoms are almost completely rejected, while B atoms still remain in the α-Fe particle. Most interesting observation in these concentration depth profile is depletion of Fe and enrichment of Zr at the α/amorphous interface as schematically shown in the inset figure. This suggests that the metastable local equilibrium is achieved at the growing interface and the particle growth is controlled by diffusion of Zr.

Figure 17 shows Ne FIM image of the Fe-7Zr-3B annealed at 973 K for 5 min. Extremely small grains can be clearly recognized. Grain boundaries are observed as discontinuity of the concentric rings (some examples are indicated by arrowheads). Amorphous like phase is also recognized between the grains, indicating that this is composed of bcc grains and remaining amorphous phase. Atom probe concentration depth profiles of the same specimen (Fig. 18) shows that there are Fe enriched and Zr enriched phases. The Zr concentration in the Zr enriched phase is almost equal to that is expected from the Fe_3Zr phase (25at.%Zr), but no diffraction evidence for the presence of equilibrium Fe_3Zr was observed in this stage. Hence, these Zr enriched phase is believed to be still amorphous. In these phases, B concentration is as high as 10 at.%, but appreciable amount of boron still remains in the α-Fe phase. On the other hand, Zr is almost completely rejected form the α-Fe phase. It should be noted that neither Zr nor B is segregated at the α/amorphous interfaces, suggesting that partitioning of Fe and B are almost completed after annealing for 5 min. at 923 K.

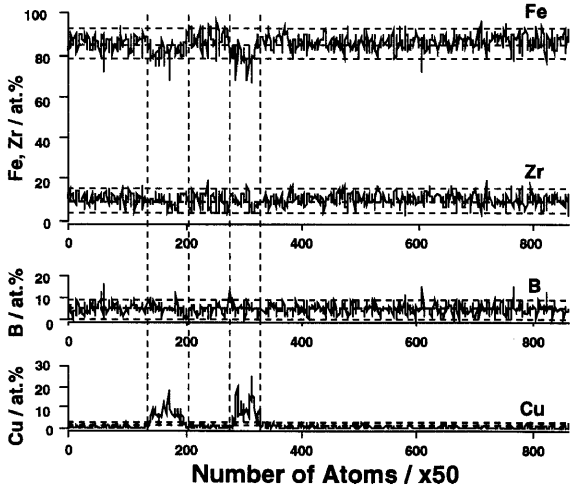

Fig. 19 Atom probe concentration depth profile of Fe-7Zr-3B-1Cu annealed at 673 K for 60 min.

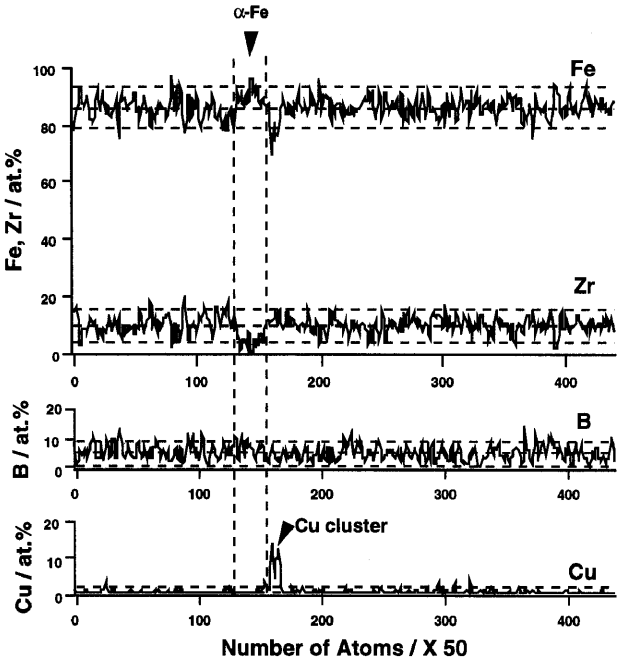

Fig. 20 Atom probe concentration depth profile of Fe-7Zr-3B-1Cu alloy annealed at 723 K for 60 min. α-Fe phase is adjacent to a Cu cluster (arrowed) indicating that α-Fe particle was heterogeneously nucleated at the Cu cluster.

4.3.2 Clustering of Cu in Fe-Zr-B-Cu amorphous alloy

Atom probe results of the as-quenched Fe-7Zr-3B-1Cu alloy also revealed that all alloying elements were homogeneously dissolved as an amorphous supersaturated solid solution [59]. After annealing at 673 K for 60 min., it was confirmed that the specimen was still amorphous, but atom probe concentration depth profiles convincingly showed that Cu atoms form clusters as shown in Fig. 19. In this figure there are two distinctly Cu enriched regions containing approximately 15 at % Cu. In Cu enriched regions, the concentrations of Zr and B are similar to those of the other uncrystallized regions, and only the concentration of Fe is decreased. From these concentration depth profiles, it is concluded that Cu atoms are negatively correlated with Fe atoms at this stage, but formation of Cu atom clusters did not affect the distributions of Zr and B.

In the case of Fe-Si-B-Nb-Cu alloy, it was shown that both Nb and Cu were required for nanocrystallization [2]. Previous studies by APFIM [34] and extended x-ray absorption fine structure (EXAFS) studies [51-53] showed that Cu formed clusters before the onset of the crystallization reaction. On the other hand, Fe-Zr-B amorphous alloy forms nanocrystalline microstructure on crystallization even without Cu [37]. However, it was reported that addition of Cu to Fe-Zr-B ternary alloy reduced the grain size further in certain alloy compositions [37]. Based on our observation, we can conclude that the role of Cu in Fe-Zr-B is similar to that in Fe-Si-B-Nb-Cu alloy and, formation of Cu clusters appears to provide additional nucleation sites of α-Fe particles during the nucleation and growth, resulting in finer grain size. In fact, evidence for direct nucleation of α-Fe particle at a Cu cluster

was found in the annealed Fe-7Zr-3B-1Cu alloy as shown in Fig. 20 [60]. The α-Fe phase (arrowed) is adjacent to the Cu cluster, indicating that α-Fe was nucleated at the Cu/amorphous interface.

4.3.3 Partitioning of Si in Fe-Zr-Si-B nanocrystalline alloy

In nanocrystalline Fe-13.5Si-9B-3Nb-1Cu alloy (FINEMET), we reported that Si partitioned into the α-Fe phase forming α-FeSi solid solution and the concentration of Si of this phase was estimated to be approximately 20 at.% [48]. Thus, it is also anticipated that Si would partition into the α-Fe phase in the nanocrystalline Fe-7Zr-4Si-2B alloy. Figure 21 shows atom probe concentration depth profiles of Fe-7Zr-4Al-2B alloy annealed at 873 K for 60 min [60]. Two phases are present in this condition: one is α-Fe phase with little solute content and the other is residual amorphous phase enriched with Zr and Si. In the figure, vertical broken lines show some of α/amorphous interfaces. From this result, the Fe concentration in the α-Fe phase is estimated to be approximately 96 at.%, containing ~2 at.% of Zr, ~1.5 at.% of Si and less than 1 at.% of B. Si is apparently rejected from the α-Fe particle during the nucleation-and-growth process from the amorphous matrix, and enriched in the residual amorphous phase. The concentration of Si and Zr in the residual amorphous matrix is approximately 7 and 17 at.%, respectively. It has been also found that B is partitioned into the residual amorphous phase, and the partitioning factor was estimated to be ~ 2.

The enrichment of Si in the residual amorphous phase will be explained assuming that there is a strong interaction between Si and Zr atoms compared to that between Si and Fe.

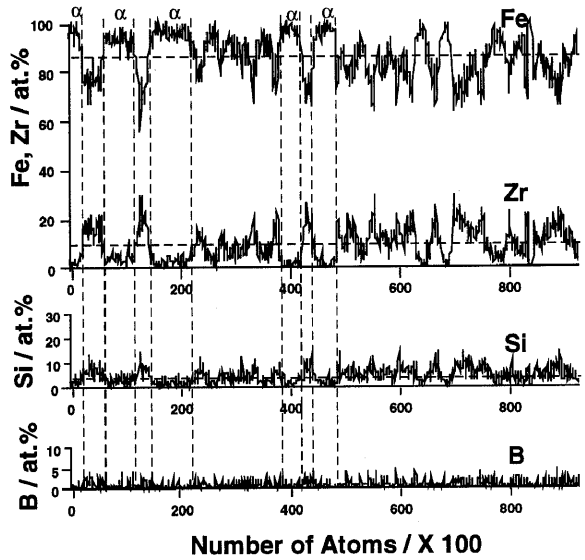

Fig. 21 Atom probe concentration depth profiles of Fe-7Zr-4Si-3B annealed at 873 K for 60 min.

The enthalpy of mixing, ΔH_{mix}, between Si and Zr for ZrSi is estimated to -18500 cal/mol, which is two times as high as that of FeSi, -9423 cal/mol [64]. Hence, Si is expected to have stronger interaction with Zr. When Zr is rejected from α-Fe, Si would be attracted to Zr enriched amorphous phase although Si has high solubility in α-Fe. Nb and Si is expected to have a strong interaction also, but Si is enriched in the α-Fe phase in the Fe-13.5Si-9B-3Nb-1Cu alloy. This may be related to higher concentration of Si and lower concentration of Nb in Fe-Si-B-Nb-Cu.

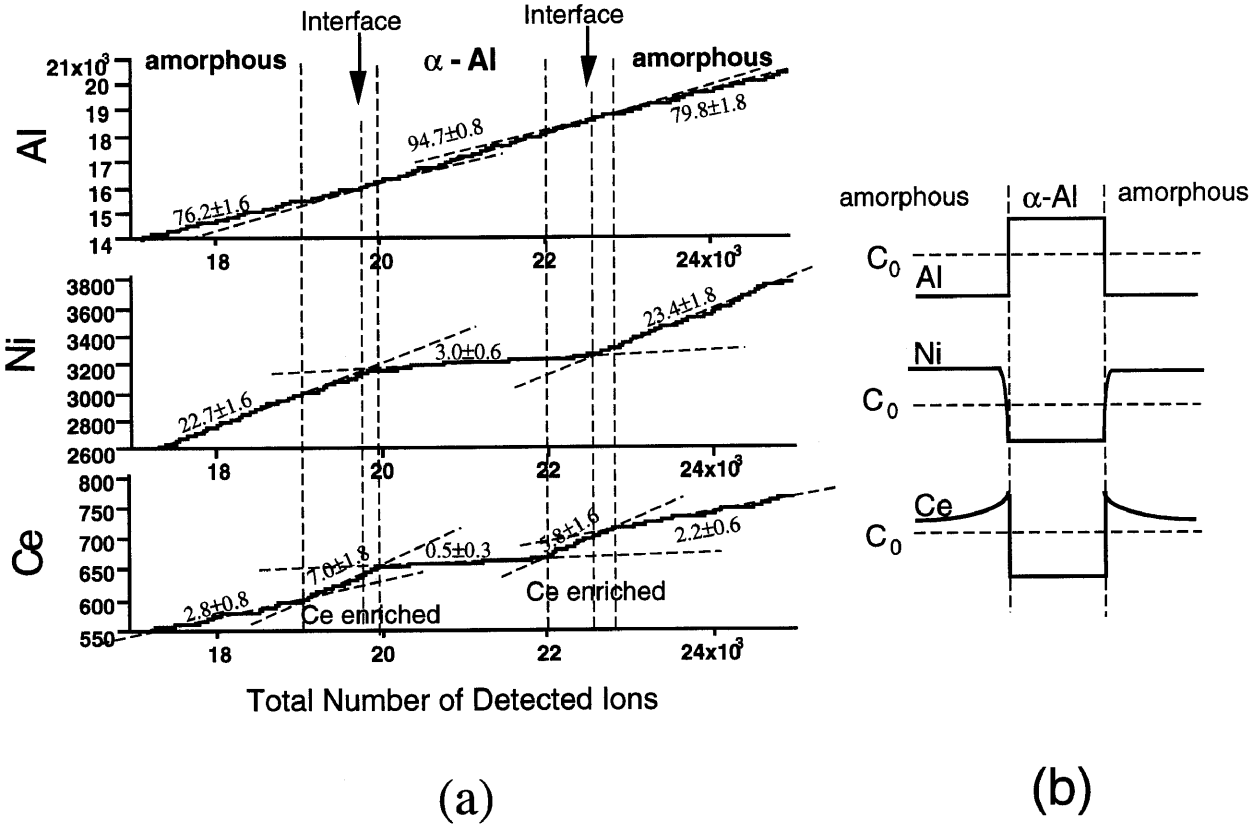

Fig. 22 (a) A integral concentration depth profile through an α-Al particle embedded in an amorphous matrix and (b) schematic illustration of the concentration depth profile. This data shows that Ce is enriched at the α/amorphous interface.

4.4 Al-Ni-Ce(-Cu)

A new family of aluminum based amorphous alloys, recently discovered by two independent groups [65, 66], show remarkably high tensile strength as well as good ductility. These amorphous alloys are based on Al-TM-RE (TM=Fe, Co, Ni, Cr; RE=Y, La, Ce, Sm, Gd, Lu and Hf), containing 80 - 92 at.% aluminum. It has been reported that the yield strength of these materials reaches as high as 800 MPa in the amorphous state, and can be increased to 1,500 MPa by partial crystallization [39,43]. The partially crystallized microstructure consists of nanoscale fcc particles embedded in an amorphous matrix. The volume fraction of these particles can be controlled by varying the cooling rate, and the yield strength reaches the maximum with a volume fraction of approximately 20% [39,40,42]. It is interesting to note that the average grain size can be controlled by substituting the transition element with Cu and Ag [43].

Isochronal DSC has shown that crystallization from the fully amorphous state to the fully crystallized state proceeds in two stages [44], as in many other nanocrystal/amorphous composite materials. Lattice parameter measurements suggest that the nanocrystalline fcc particles are the α-Al phase [39,43], but this remains unconfirmed by other techniques. It has also been reported that the crystallization kinetics are very fast and only the growth stage is observed in DSC [67, 68]. This suggests that certain heterogeneities that may act as nucleation sites for crystallization are present in the melt-spun alloys.

Atom probe analysis results [69] showed that two distinctly different phases are present in the partially crystallized Al-10Ni-3Ce alloy; one is α-Al containing approximately 98 % Al and the other is the matrix amorphous phase containing approximately 25 % Ni and 3 % Ce. Figures 22 (a) shows the number of Ce atoms plotted as a function of the total number of detected atoms. In this diagram, the slope of the plot represents the local concentration of the alloy element, and the x axis corresponds to the depth. By a tangent construction, we can determine the average local concentration of the alloy. The location of the interface is determined from the aluminum concentration change. The concentration of each element between the dotted lines is shown in the diagram. Both Ni and Ce atoms are almost completely rejected from the α-Al phase. Note that Ce atoms are enriched within distance of less than ~ 3 nm (1000 atoms) at the α/amorphous interface. The concentration profile deduced from this is schematically shown in Fig. 24 (b). Although both Ni and Ce are rejected from the α-Al phase, only Ce is enriched at the interface.

As there is virtually no solubility of Ni or Ce in the α-Al phase, the complete rejection of them from the crystallized α-Al particles is predictable. It is interesting to note that only Ce segregates at the α/amorphous interface (Fig. 22), whereas Ni does not. A possible explanation is the slower diffusivity of Ce. The atomic radius of Ce is much larger than the other solute elements (28 % larger than Al) and this leads us to speculate that the diffusivity of Ce in this alloy may be lower than those of Al and Ni by orders of magnitude. Hence, during the growth of the α-Al particles, the rejected Ce atoms are enriched at the interface and it has to drag Ce for further growth. This would effectively slow down grain growth.

An atom probe concentration depth profile obtained from the as-quenched Al-7Ni-3Cu-3Ce amorphous alloy indicated that compositional fluctuations of Cu and Ce are present even

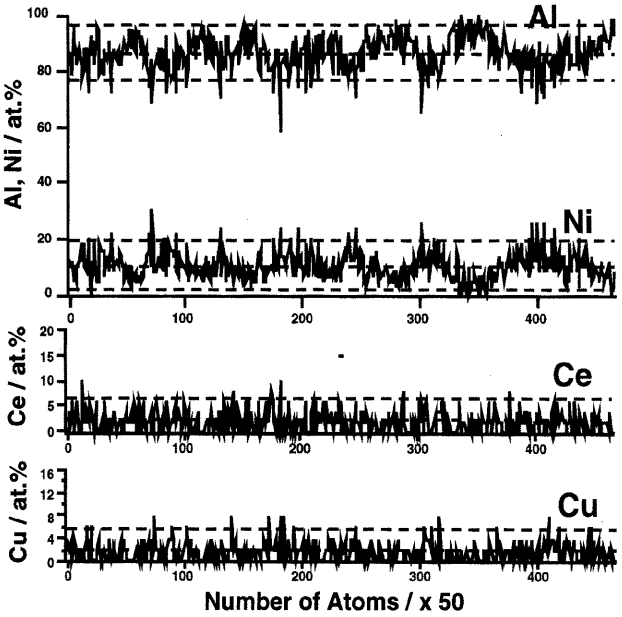

Fig. 23 Atom probe concentration depth profile of an as-quenched Al-7Ni-3Cu-3Ce alloy.

in the melt spun amorphous state as shown in Fig. 23 [70]. The presence of such heterogeneities in the as-quenched state may lead to a high number density of nuclei for crystallization. For growth of the fcc particles, Ce, Cu and Ni have to be rejected from the α-Al phase, but Ce diffuse slower than the other elements, so it enriches at the α/amorphous interface.

5. Phase decomposition in Co-Cr sputter-deposited thin films

Co-Cr alloy is the fundamental system employed in current longitudinal high density recording media, such as Co-Cr-Ta and Co-Cr-Pt [71, 72]. Co-Cr alloy thin film are also considered to be one of the most promising media for perpendicular recording [73]. It is well known that the magnetic properties of the thin film recording media depend on sputtering parameters, such as bias voltage, gas pressure and substrate temperature. One such example is the increase in coercivity and the decrease in media noise when Co-Cr based films are deposited on heated substrates [74,75]. The underlying mechanisms of such magnetic property changes, however, are not well understood.

Magnetic measurements indicate that there may be compositional heterogeneities in Co-Cr binary alloy thin films [76-80]. For example, Fisher *et al.* [77] found that the saturation magnetization and Curie temperature of sputtered thin films were higher than those of bulk materials with the same mean composition. Subsequently, many investigations have attempted to confirm the presence of compositional heterogeneities in these alloy thin films [78-82]. It has been suggested that such compositional heterogeneities may be explained by grain boundary segregation of Cr. In this model, each columnar grain is thought to be magnetically isolated from neighboring grains by a Cr enriched grain boundary phase and thus could function as the minimum unit of the recording bit [81]. In order to test this model, several analytical electron microscopy studies using x-ray energy dispersive spectroscopy (EDS) were performed [82-84]. However, limitations in the spatial resolution of these

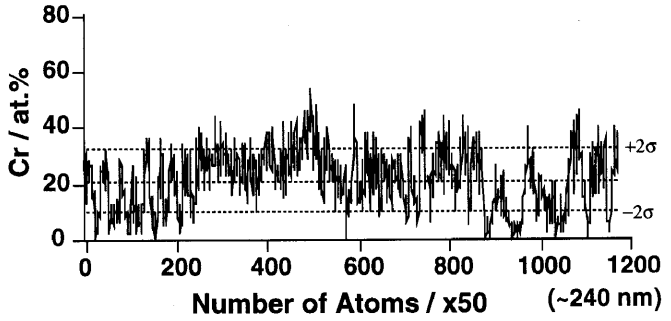

Fig. 24 One dimensional atom probe concentration depth profile of Co-22at.%Cr alloy thin film sputter-deposited at 573 K.

methods, which employ a focused electron beam, make it difficult to obtain quantitative results that provide evidence for the grain boundary segregation or chemical heterogeneities within the small grains in sputtered thin films.

It is impossible to observe compositional heterogeneities in these films by structure factor contrast using transmission electron microscopy (TEM), since the atomic scattering factor of Cr is very similar to that of Co. Maeda *et al.* [85-87], however, observed a chrysanthemum-like pattern (CP) structure within the grains of Co-Cr thin films deposited on heated substrates by chemically etching the Co in the Co-Cr films. They proposed that the bright contrast in this CP structure represented preferential dissolution of regions which were Cr depleted prior to etching. Based on this interpretation, they concluded that fine compositional fluctuations existed *within* each grain. Many subsequent results were published supporting the presence of compositional heterogeneities within the grains. These included analytical TEM studies [88], nuclear magnetic resonance (NMR) measurements [89,90], thermomagnetic analysis [91,92], small angle neutron scattering (SANS) studies [93] and atom probe investigations [94-99].

Figure 24 shows a one dimensional atom probe concentration depth profile of Co-22at.%Cr thin films sputter deposited at 473 K, which convincingly showed that the films prepared at elevated temperatures were composed of ferromagnetic and paramagnetic phases of comparable dimensions. The specimen was prepared along the direction of the film, so the concentration depth profile represents fluctuations in the Cr concentration in the planar direction of the film. One phase is rich in Cr (~30 - 40 at.%Cr), and the other is depleted in Cr (~5 - 10 at.%Cr). The sizes of Cr and Co enriched regions are comparable (~8 nm). The Curie temperature becomes lower than room temperature when the Cr concentration exceeds 25 at.%, hence the Cr enriched phase is paramagnetic and the Co enriched region is ferromagnetic. As the size of the paramagnetic phase is several nanometers, each ferromagnetic phase is believed to be isolated magnetically. The scale of the compositional fluctuation is significantly smaller than that of the grains, hence it is concluded that compositional fluctuations are present within the grains. Such compositional inhomogeneity cannot be explained by equilibrium grain boundary segregation and it is suggested that this is caused by phase separation which occurred during the sputtering process. The thin films deposited at the ambient temperature did not show such long range fluctuation of Cr concentration [96]. This indicates that sputter deposition on a heated substrate enhances the kinetics of decomposition, because high energy ions can migrate on the growing surface by a surface diffusion mechanism. In this case, the two phase state, which will never be achieved in the bulk specimen, can be realized by the sputter deposition at elevated temperatures.

While the conventional atom probe data convincingly showed the presence of the compositional heterogeneity, it does not provide any information on the morphology of the phase. Hence, in order to visualize the morphology of the ferromagnetic particles, three dimensional atom probe analysis was performed. Figures 25 (a) and (b) show a three dimensional concentration mapping and isoconcentration contours which were constructed by connecting concentration data points of 75at.%Co, respectively. The three dimensional concentration mapping (Fig. 25 (a)) shows there is significant fluctuation in Co concentration. It can be clearly seen that the Co enriched and Cr enriched phases form a lamellar structure. The thickness of the Cr enriched lamellae is approximately 5 nm. The isoconcentration contours correspond to the interfaces between paramagnetic and ferromagnetic phases. TEM observations did not reveal any evidence for the presence of multiple crystallographic phases,

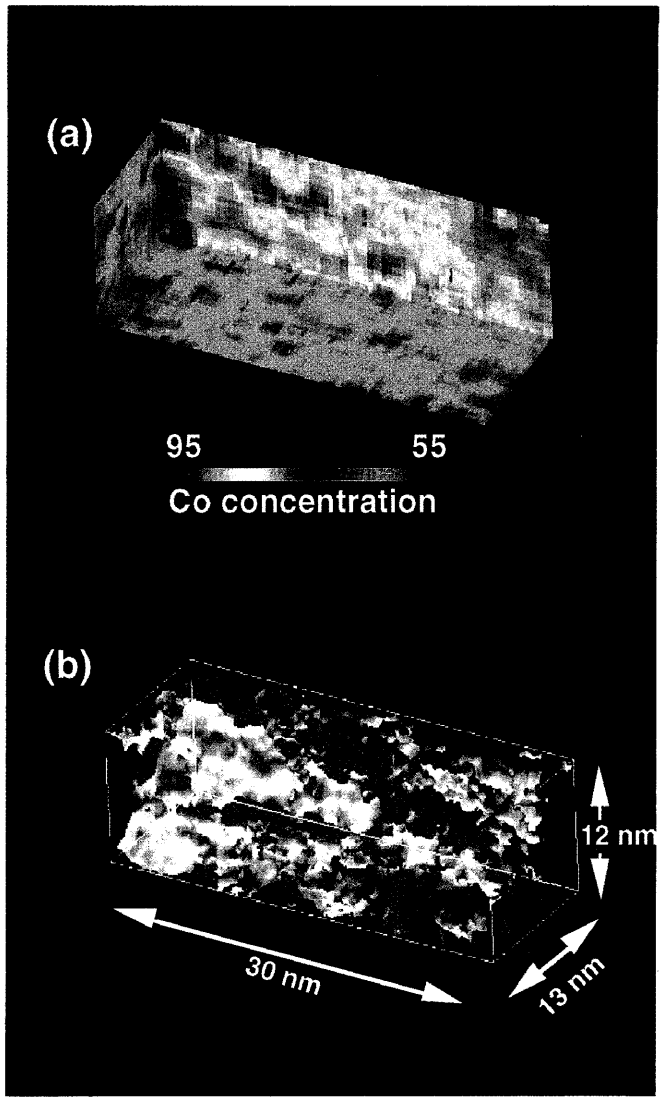

Fig. 25 Three dimensional atom probe data collected form a interior region of a grain. (a) Gray scale three dimensional concentration mapping and (b) isoconcentration contour of 75at.%Co. This surface corresponds to interface between the paramagnetic and ferromagnetic phases.

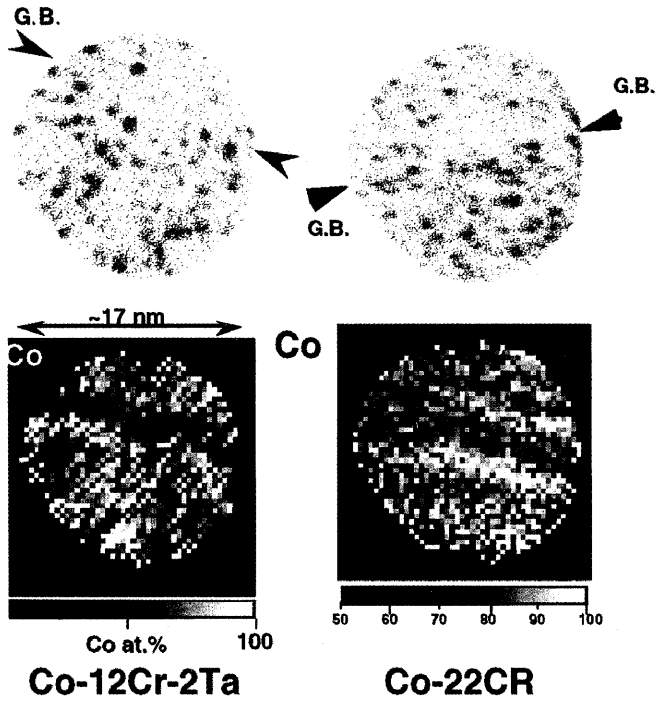

Fig. 26 Digital FIM images of Co-12Cr-2Ta and Co-22Cr thin films containing a grain boundary. Corresponding concentration mappings of Co are shown. The films were sputter deposited at 500 K.

so both the Co enriched and depleted phases are hcp ε-Co.

This work directly reveals compositional heterogeneity within grains of the Co-Cr thin films sputter-deposited at elevated temperatures. In addition, the three dimensional compositional mapping shows convincingly that the ferromagnetic and paramagnetic phases both exist in a lamellar structure. The lamellae of the Co enriched phase are also completely separated from each other by the lamellae of the Cr enriched paramagnetic phase, whose width is 5 - 10 nm. This thickness is believed to be sufficient to suppress exchange interactions between neighboring ferromagnetic regions. It also should be noted that if the ferromagnetic phase were composed of spherical particles less than ~10 nm in diameter, the film would exhibit superparamagnetic behavior. These phases, however, form a lamellar structure within the grain, as shown in Fig. 25, and hence the ferromagnetic phase will be more resistant to thermal fluctuations due to shape anisotropy even though they are only a few nanometers in width.

The origin of the lamella-like compositional heterogeneity is proposed to be due to phase decomposition which progresses during film deposition at elevated temperatures [99]. Based on the phase diagram calculated by Hasebe et al. [100], the isostructure two phase field appears at a temperature region below approximately 500 K for the Co-22at.%Cr. Hence, phase decomposition is expected to take place in the low temperature region for the Co-22at.%Cr solid solution. In the bulk, however, such phase decomposition would never occur, due to sluggish volume diffusion in this temperature range. The phase decomposition would be kinetically possible only during the film deposition process at the film surface, because during sputtering atoms have high kinetic energies and are mobile at the surface upon deposition. By elevating the substrate temperature to around 600 K, phase separation would progress two dimensionally by surface diffusion, and this would cause a lamellar structure composed of the alternating ferromagnetic and paramagnetic phases. When the substrate temperature is lower, the kinetics for surface diffusion are not fast enough and a compositionally uniform film should grow.

It has been well known that ternary addition of Ta is particularly effective in increasing the coercivity and decreasing the media noise, and this makes Co-Cr-Ta alloy thin films attractive as recording media [71,101]. However, the underlying mechanism of the effect of ternary addition of Ta is not really understood. One proposed mechanism is formation of nonmagnetic phase along grain boundaries, leading to isolation of individual ferromagnetic grains. A recent elemental mapping study using electron energy loss spectroscopy (EELS) [103] clearly showed that Cr enriched phase is present along the grain boundaries and within grains, but the mapping of Ta has not been successful using this method. In order to understand the effect of Ta addition to the microstructure, it is necessary to understand the distribution of Ta as well as that of Cr in Co-Cr-Ta films. Figures 26 show digital FIM images of Co-22Cr and Co-12Cr-2Ta thin films containing a grain boundary and two dimensional concentration maps obtained from the corresponding area. In Co-22Cr alloy thin films, enrichment of Cr has not been

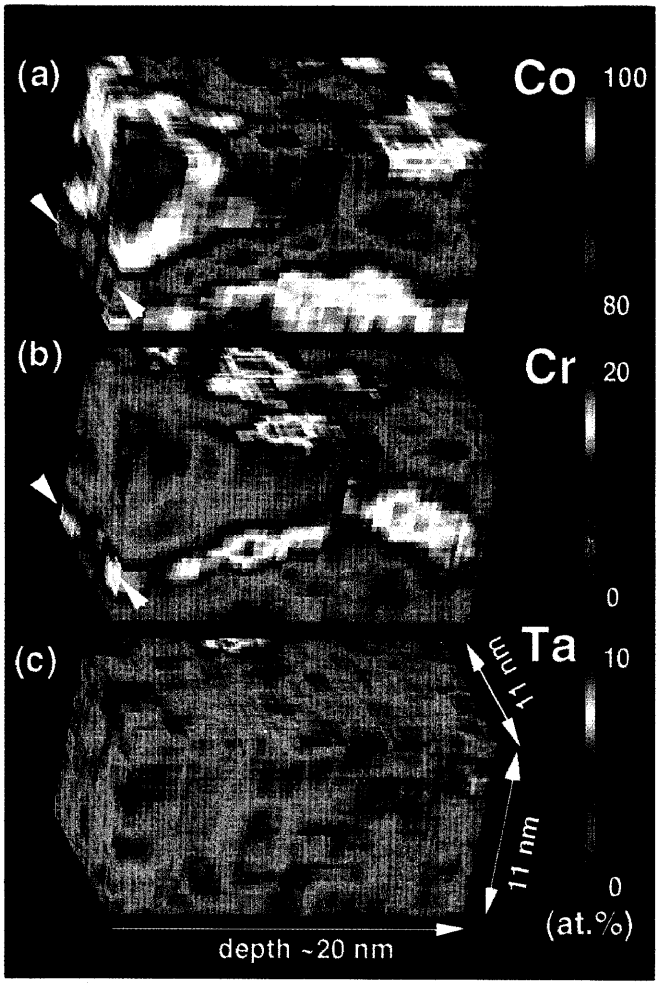

Fig. 27 Three dimensional concentration mappings of (a) Co, (b) Cr and (c) Ta. The left side surface of the parallelepiped is the initial surface of the specimen and the arrowheads in (a) and (b) show the grain boundary observed in Fig. 27 (b). Cr-enriched grain boundary phase envelopes Co-enriched grains. There is slight fluctuation in Cr concentration even within the grains. Ta distribution appears uniform.

recognized along the grain boundary, while in Co-12Cr-2Ta film, Cr is significantly enriched along the grain boundary. This suggests that addition of Ta somehow enhance formation of grain boundary phase enriched in Cr along grain boundaries. Three dimensional elemental mapping shown in Fig. 27 clearly show that Cr enriched grain boundary phase envelopes Co enriched grain. Note that there is fluctuation of Cr even within grains. It should also be noted that Ta atoms themselves are not enriched at the grain boundaries. This indicates that Ta dissolution in Co-Cr solid solution somehow enhance kinetices of phase separation.

6. Magnetoresistance and phase decomposition in Cr-Fe alloys

Giant magnetoresistance (GMR) was reported for the first time in Cr/Fe thin films with the multilayer structure [104]. Since then, this phenomenon has been observed in many metallic multilayers which are composed of nonmagnetic and ferromagnetic thin layers of a few nanometers [105-108]. A recent discovery of GMR in alloy thin films with heterogeneous structure, in which nanoscale ferromagnetic particles are distributed in the nonmagnetic matrix phase, has stimulated research into non-multilayer type GMR [109,110]. This has been reported in the alloy systems composed of nonmagnetic and ferromagnetic elements with negligible solubilities like Cu-Co, Ag-Fe, Ag-Co etc [111]. Moreover, it has been recently shown that a similar phenomenon is observed in melt spun ribbons of Cu-Co [112-114] as well as in bulk Cu-Ni-Fe alloy [115]. The origin of MR in these heterogeneous alloy films is believed to be similar to that of multilayer type GMR, i.e. the spin dependent electron scattering by the ferromagnetic particles. Although this type of GMR has been reported in many binary alloy systems, the Cr-Fe system has not been examined in the thin film or bulk alloy form with heterogeneous structure. The Cr-Fe system is quite different from the other systems where GMR has been reported in the heterogeneous structure in the following points: (1) the equilibrium solid solution exists above 1094 K in the entire concentration region, (2) it has a large miscibility gap below 1094 K, but the solubility limit of each side is as much as 10 at.% even at 700 K. Phase separation is expected to occur by aging the supersaturated solid solution at temperatures below the miscibility gap, although the kinetics of the decomposition is expected to be very slow below 800 K due to the low bulk diffusivity. In order to correlate GMR with phase decomposition, Okano et al. studied GMR behavior and characterized the corresponding microstructures by APFIM [116].

Variations of the MR ratios of Cr-25at.%Fe bulk alloy with three different heat treatment conditions (as-quenched, aged for 400 h and 2600 h at 773 K) are shown in Fig. 28 [116]. In this figure, the values of $\Delta\rho/\rho$ at 4.2, 77 and 290 K were plotted as a function of applied magnetic field. Large negative magnetoresistance is observed in all specimens at 4.5 K. MR decreases monotonically to 5.8 kOe, but the magnetoresistance change does not seem to saturate even at

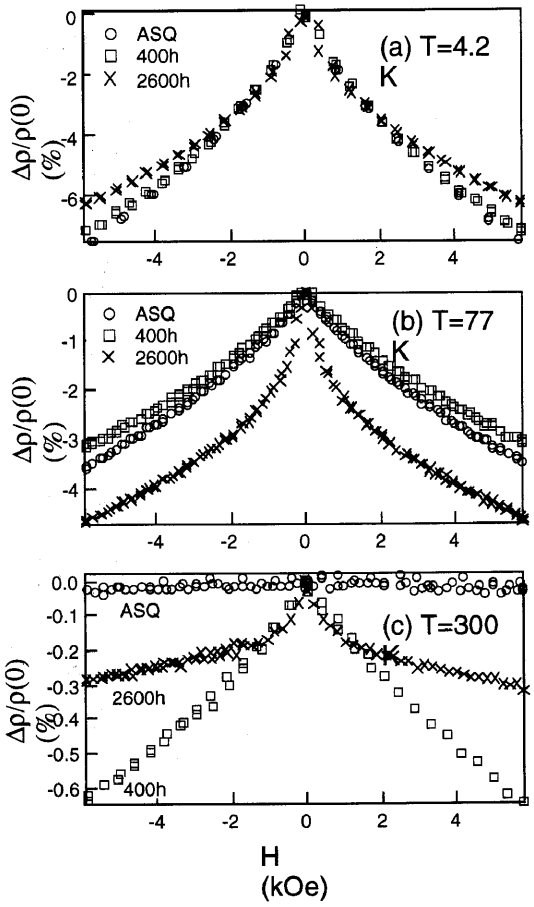

Fig. 28 MR ratios, $\Delta r/r$ at 5.8 kOe, of as-quenched Cr-25at.%Fe (referred to as ASQ), the same alloy annealed at 773 K for 400 h. (referred to as 400 h) and for 2600 h. (referred to as 2600 h). Measured at (a) 4.5 K, (b) 77 K and (c) 300 K.

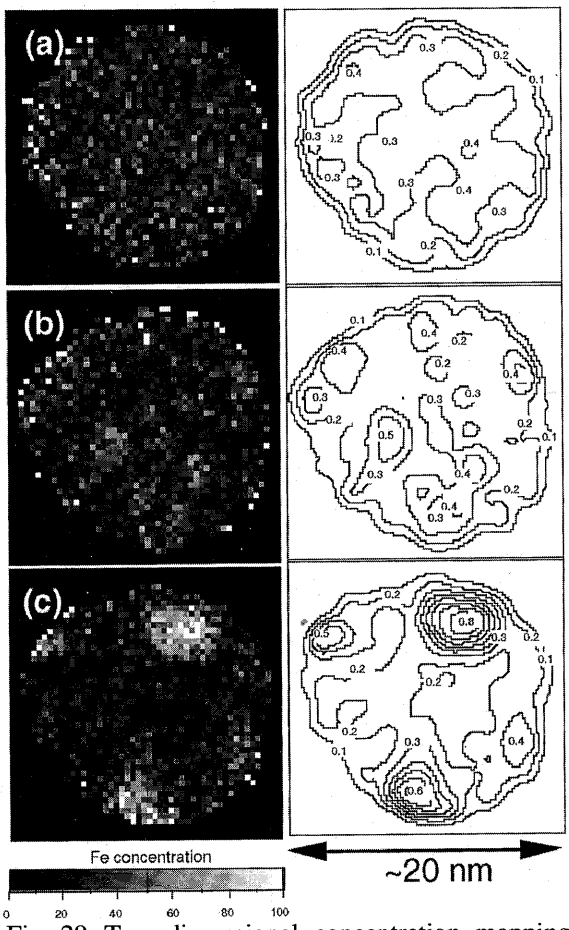

Fig. 29 Two dimensional concentration mapping of Cr-25at.%Fe alloy (a) as-quenched, (b) annealed at 773 K for 400 h and (c) annealed at 773 K for 2600 h. the gray scale corresponds to the concentration of Fe.

5.8 kOe. The MR dependence on the heat treatment is not prominent at 4.5 K and all samples show similar behavior. However, it may be noted that the MR ratio at 5.8 kOe becomes smaller as the annealing time becomes longer. The tendency is entirely different at 77 K as shown in Fig.29 (b). The highest MR ratio was obtained in the 2600 h specimen and the as-quenched and 400 h specimens show similar MR behavior. The MR change at the low field region is more noticeable in the 2600 h specimen. At 300 K, the difference becomes more prominent. Although MR does not appear in the as-quenched specimen, the sample aged for 400 h. shows unsaturated monotonic MR changes. The specimen aged for 2600 h. shows a small but steep MR change at lower than 2 kOe, but it almost saturates at that field.

In order to understand these peculiar MR behaviors, the nature of Fe clusters in the alloy as a function of annealing time has been characterized by APFIM. Fig. 29 shows two dimensional concentration mappings and their corresponding isoconcentration contours of (a) as-quenched specimen and of specimens (b) annealed at 773 K for 400 h and (c) annealed at 773 K for 2600 h. In this figure, local concentrations of Fe are displayed with a gray scale. The concentration mapping of the as-quenched sample show only statistical concentration fluctuations and no Fe rich particles are observed. In the specimen annealed at 773 K for 40 h., fluctuations in Fe concentration can be clearly recognized. However, the interface between the Fe-enriched region and the matrix is still not clear. The isoconcentration contours indicate that the maximun concentration of the Fe-enriched region is only 50at.%Fe, which is significantly lower than the equilibrium value, 80at.%Fe. The concentration mapping indicates that the Fe-enriched regions are interconnected. This type of concentration modulation is expected in the early stage of spinodal decomposition. In the specimen annealed for 2600 h., discrete Fe rich particles are recognized. The concentration of Fe in the particles are ~80at.%Fe, which is close to the thermal equilibrium value. Isoconcentration contours indicate that the concentration change at the particle/matrix interfaces are much more discrete that those in the previous two specimens. Note that ~20at.%Fe are still remain in the matrix.

Based on these atom probe results, the distribution of spins of Fe atoms as well as the spontaneous magnetization of ferromagnetic particles can be schematically represented as Fig. 30, where small arrows indicate the spins of independent Fe atoms and large arrows indicate the spontaneous magnetization of the single domain ferromagnetic particles. The aggregates of arrows represent ferromagnetically coupled spin clusters. The as-quenched alloy is spin cluster glass, in which a mixture of ferromagnetically and antiferromagnetically coupled spin clusters is present, while the chemical composition is homogeneous on a macroscopic scale but fluctuate in a statistical sense. The spins of the ferromagnetic clusters are easily rotated by the application of a magnetic field, but the individual spins frozen as spin glass do not rotate easily as they are coupled by the RKKY interaction. The latter results in the unsaturated type MR, because the direction of the spin will not be aligned with the application of the usual strength of magnetic field. As temperature increases, the direction of the spin will be disturbed by thermal fluctuations and it will become impossible to align spins by the application of an external magnetic filed. However, the direction of spontaneous magnetization will still be aligned by an applied magnetic field, because the thermal energy is not large enough to perturb the direction of the spontaneous magnetization. Hence, at higher temperatures, the MR originated from spin glass disappears, but the MR originated from magnetic particles remains. The MR change observed in Fig. 8 can be qualitatively explained by the interplay of MR's originated from ferromagnetic particles, spin and cluster glasses and their thermal agitation. Atom probe analysis clearly showed how much fraction of solute are dissolved in the matrix phase which cause spin glass effect at low temperatures and how much Fe are consumed for the formation of ferromagnetic particles. Also, it offered valuable information regarding the particle size, interparticle distance, density , and composition of ferromagnetic particles, all of which are key factors in controlling the MR in the heterogeneous alloy structure. Nanostructure characterization by atom probe analysis of these heterogeneous magnetic alloys will yield crucial information on the mechanisms of various magnetic properties.

7. Other Applications

Most popular applications that the atom probe technique has been employed is microstructural characterization of steels. This is because steel has been traditionally the most important metallic materials for structural applications and also because carbon plays critical role in microstructural evolution. Even today, no other microanalytical techniques can beat the quantitative analytical capability of light elements that can be achieved by an atom probe. Although numerous atom probe researches have been carried out to solve various problems in steels, one classical question concerning paraequilibrium at interfaces has not been tested. Since carbon is dissolved interstitially, the diffusivity of carbon is magnitudes of order higher than those of substitutional solute elements, such as Si, Mn. Si and Mn are common solute elements added in low alloy steels. The concept of paraequilibrium [117] predicts carbon partitioning

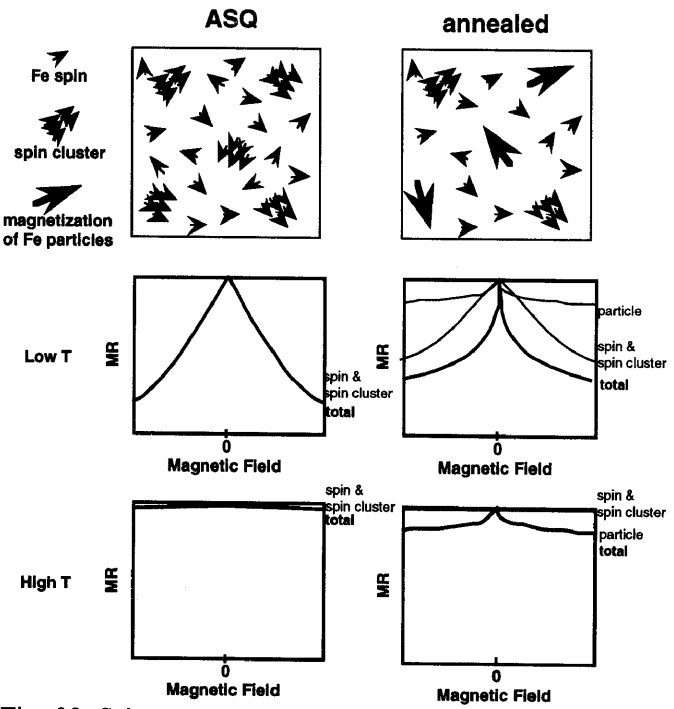

Fig. 30 Schematic drawings of MR curves expected from three types of scattering sources, i.e. individual spins of Fe atoms, spin clusters and ferromagnetic particles.

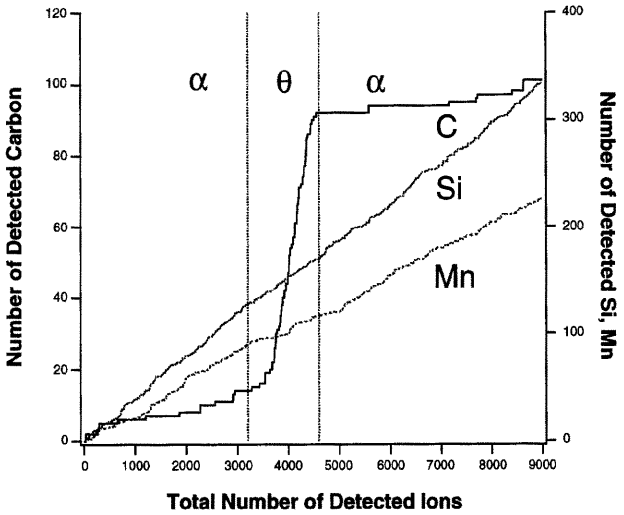

Fig. 31 Concentration depth profile across α/θ/α interface. Note that only carbon is enriched in the cementite phase, while no partitioning of Si and Mn are observed.

without partitioning of substitutional solute in growing ferrite/austenite interface. In order to test this prediction, it is desired to observe ferrite/austenite interface of low carbon steels, but the microstructure scale of ferrite precipitation from austenite is too large to be tested with the atom probe technique. Babu et al. [118,119] studied chemical composition changes during the nucleation and growth of cementite from the tempered martensite, and found that no partitioning of Mn and Si occurred in the early stage of cementite precipitation in a Fe-1.84C-3.84Si-2.95Mn (at.%) low alloy steel as shown in Fig. 31. At the interface, no segregation of Mn nor Si was detected, they concluded that this is evidence for paraequilibrium growth of cementite. Later, a similar study has been performed by Thomson and Miller [97] using Fe-Cr-Mo-C steel, and they obtained the similar result supporting the paraequilibrium growth of cementite.

Since atom probe has an atomic layer resolution in the depth analysis, if an alloy has an ordered structure, chemical change corresponding to the ordered structure can be detected. Using this capability, it is possible to determine site occupancy of solute elements in ordered alloys. Hono et al. [121,122] and Numakura et al. [123, 124] attempted this method for determining site occupation probability of Cu and Ge in Ni_3Al. It turned out that applicability of this method is limited for only some alloy systems, in which field evaporation of the ordered plane goes smoothly. In L1o ordered lattice, such as TiAl, it was impossible to apply the atom probe method for determination of sites of ternary elements, since evaporation field Ti and Al is very different.

8. Concluding Remarks

IMR has a rich tradition in the development of many metallic materials such as amorphous alloys, magnetic materials, nanocrystalline alloys and intermetallics. When the authors started their atom probe research at this institute, we noticed that we built the right instrument in the right place. Numerous interesting materials for atom probe analysis were provided from colleagues in the institute. In particular, we felt that we were very fortunate that we could access the hottest amorphous materials before anybody else in the world. This stimulated some research on the microstructural evolution in amorphous and nanocrystalline alloys. Research on magnetic materials were stimulated by our neighbor, Professor Fujimori's laboratory members, and we were able to combine both magnetic measurement and microstructural characterization at the same time using the facilities in different groups. Inter-laboratory collaboration has worked in the ideal way for our atom probe research activities since 1990. The authors hope that the new tradition which was created at this laboratory will continue into the next generation.

Acknowledgment

We wish to thank all who contributed to the works reviewed in this article. These include Dr. S. S. Babu, Professor H. Fujimori, Dr. N. Hasegawa, Professor T. Hashizume, Professor A. Inoue, Mr. J.-L. Li, Mr. J. Nishimaki, Dr. H. Numakura, Mr. R. Okano, Professor I. J. Polmear, Dr. S. P. Ringer, Dr. N. Sano, Mr. T. Saeda, Dr. I. Szabo, Professor K. Takanashi, Professor A. P. Tsai, Mr. Q. Wang, Mr. K. Yeh, Ms. Y. Zhang.

References

1. M. K. Miller and G. D. W. Smith, Atom-Probe Microanalysis: Principles and Applications to Materials Problems, MRS, Pittsburgh, 1989.
2. A. Cerezo, T. J. Godfrey and G. D. W. Smith, Rev. Sci. Instrum, **59**, 862 (1988).
3. K. Hono, T. Hashizume and T. Sakurai, Surf. Sci. **266**, 506 (1992).
4. T. Abe, K. Miyazaki and K. Hirano, Acta Metall., **30**, 357 (1982).
5. M. Wada, H. Kita and T. Mori, Acta metall., **33**, 1631 (1985).
6. K. Hirano and K. Hono, Ann. Rev. Mater. Sci., **18**, 351 (1988).
7. K. Hono, R. Okano, T. Saeda and T. Sakurai, Appl. Surf. Sci. **87/88**, 453 (1995).
8. P. Jacobaeus, J. U. Madsen, F. Kragh and R. M. J. Cotterill, Phil. Mag. B, **41**, 11 (1980).
9. B. W. Krakauer, J. G. Hu, S.-M. Kuo, R. L. Mallick, A. Seki, D. N. Seidman, J. P. Baker and R. J. Loyd, Rev. Sci. Instrum. **61**, 3390 (1990).
10. N. Hasegawa, K. Hono, R. Okano, H. Fujimori and T. Sakurai, Appl. Surf. Sci. **67**, 407 (1993).
11. J. A. Taylor, B. A. Parker and I. J. Polmear, Metal Sci. **12**, 439 (1978).
12. B. C. Muddle and I. J. Polmear, Acta Metall. **37**, 777 (1989).
13. I. J. Polmear and R. J. Chester, Scripta Metall, **23**, 1213 (1989).
14. F. W. Gayle, F. H. Heubaum and J. R. Pickens, Scripta Metall. Mater., **24**, 79 (1990).
15. N. Sano, K. Hono, T. Sakurai, and K. Hirano, Scripta Metall. Mater. **25**, 491 (1991).
16. K. Hono, N. Sano, S. S. Babu, R. Okano and T. Sakurai, Acta metall. mater. **41**, 829 (1993).
17. S. S. Babu, K. Hono, R. Okano and T. Sakurai, Appl. Surf. Sci. **67**, 361 (1993).
18. J. M. Howe, Phil. Mag. Lett., **70**, 111 (1994).
19. K. Hono, T. Sakurai and I. J. Polmear, Scripta Mater. **30**, 695 (1994).

20. S. P. Ringer, K. Hono, I. J. Polmear and T. Sakurai, Acta Mater. **44**, 1883 (1996).
21. S. Abis, P. mengucci and G. Riontino, Phil. Mag. **70B**, 851 (1994).
22. R. Okano, K. Hono and T. Sakurai, unpublished work.
23. S. P. Ringer, K. Hono, I. J. Polmear and T. Sakurai, Proc. Inter. Conf. Solid→Solid Phase Transformations, eds. W. C. Johnson, J. M. Howe, D. E. Laughlin, W. A. Soffa, pp. 165, (TMS, Warrendale, Pennsylvania, 1994).
24. S. P. Ringer, K. Hono and I. J. Polmear, Proc. 4th Inter. Conf. on Aluminum Alloys, eds. T. H. Sanders Jr. and E. A. Starke Jr., (Georgia Inst. of Technology, USA), Vol. I, pp. 574 (1994).
25. J. M. Silcock, J. Inst. Met. **89**, 203 (1960-61).
26. S. P. Ringer, K. Hono, I. J. Polmear and T. Sakurai, Appl. Surf. Sci., **94/95**, 253 (1996).
27. S. P. Ringer, K. Hono, I. J. Polmear and T. Sakurai, Scripta Mater. **36**, 517 (1997).
28. I. J. Polmear, Trans AIME, **230**, 1331 (1964).
29. S. P. Ringer, K. Hono and T. Sakurai, Metall. Mater. Trans. A, **26A**, 2207 (1995).
30. G. Edwards, K. Stiller and G. L. Dunlop, Appl. Surf. Sci., **76/77**, 219 (1994).
31. K. Hono, S. S. Babu, K. Hiraga, R. Okano and T. Sakurai, Acta Metall. Mater. **40**, 3027 (1992).
32. G. Schmitz, K. Hono and P. Haasen, Acta Metall. Mater. **42**, 201 (1994).
33. Y. Yoshizawa, S. Oguma and K. Yamauchi, J. Appl. Phys. **64**, 6044 (1988).
34. Y. Yoshizawa and K. Yamauchi, Mater. Trans. JIM, **31**, 307 (1990).
35. N. Hasegawa and M. Saito, J. Mag. Mag. Mater. **103**, 274 (1992).
36. K. Suzuki, N. Kataoka, A. Inoue, A. makino and T. Masumoto, Mater. Trans. JIM, **31**, 743 (1990).
37. K. Suzuki, A. Makino, A. Inoue and T. Masumoto, Sci. Rep. RITU, **A39**, 133 (1994).
38. S. Hirosawa, H. Kanekiyo and M. Uehara, J. Appl. Phys. **73**, 6488 (1993).
39. Y.-H. Kim, A. Inoue and T. Masumoto, Mater. Trans. JIM, **31**, 747 (1990).
40. Y.-H. Kim, A. Inoue and T. Masumoto, Mater. Trans. JIM, **32**, 599 (1991).
41. A. Inoue, Y-H. Kim and T. Masumoto, Mater. Trans. JIM, **33**, 487 (1992).
42. A. Inoue, Y. Oorio, Y. H. Kim and T. Masumoto, Mater. Trans. JIM, **33**, 669 (1992).
43. H. Chen, Y. He, G. J. Shiflet and S. J. Poon, Scripta Metall. Mater. **25**, 1421 (1991).
44. U. Herold and U. Köster, Proc. 3rd Inter. Conf. Rapidly Quenched Metals, ed. by B. Cnator, Brighton, Metals Society, London, 1978, pp. 281.
45. G. Herzer, IEEE Trans. Mag. **25**, 2227 (1989).
46. G. Herzer, IEEE Trans. Mag. **26**, 1379 (1990).
47. K. Hono, A. Inoue and T. Sakurai, Appl. Phys. Lett. **58**, 2180 (1991).
48. K. Hono, K. Hiraga, Q. Wang, A. Inoue and T. Sakurai, Acta Metall. Mater. **40**, 2137 (1992).
49. K. Hono, J-L. Li, Y. Ueki, A. Inoue and T. Sakurai, Appl. Surf. Sci. **67**, 398 (1993).
50. S. H. Kim, M. Matsuura, M. Sakurai and K. Suzuki, Jpn. J. Appl. Phys. **32**, 676 (1993).
51. J. D. Ayers, V. G. Harris, J. A. Sprague and W. T. Elam, IEEE Trans. Mag. **29**, 2664 (1993).
52. J. D. Ayers, V. G. Harris, J. A. Sprague and W. T. Elam, Appl. Phys. Lett. **64**, 974 (1994).
53. N. Hasegawa, N. Kataoka, K. Hiraga and H. Fujimori, Mater. Trans. JIM, **33**, 632 (1992).
54. N. Hasegawa, M. Saito, A. Kojima, A. Makino, Y. Misaki and T. Watanabe, J. Mag. Soc. Japan. **14**, 319 (1990).
55. K. Hono, N. Hasegawa, S. S. Babu, H. Fujimori and T. Sakurai, Appl. Surf. Sci. **67**, 391 (1993).
56. M. Wada, K. Hosoi and O. Nishikawa, Acta Metall. **30**, 1005 (1982).
57. K. Y. Kim, T. H. Noh, I. K. Kang and T. Kang, Mater. Sci. Eng. **A179/180**, 552 (1994).
58. Y. Zhang, K. Hono, A. Inoue, A. Makino and T. Sakurai, Acta Metall. Mater. **44**, 1497 (1996).
59. Y. Zhang, K. Hono, A. Inoue and T. Sakurai, Scripta Metall. Mater. **34**, 1705 (1996).
60. Y. Zhang, K. Hono, A. Inoue and T. Sakurai, Appl. Phys. Lett. **69**, 2128 (1996).
61. Y. Zhang, K. Hono, A. Inoue and T. Sakurai, to be published.
62. Y. Hirotsu, M. Uehara and M. Ueno, J. Appl. Phys. **59**, 3081 (1986).
63. M. Nakamura, Y. Hirotsu, K. Anazawa, A. Makino, A. Inoue and T. Masumoto, Mater. Sci. Eng. **A179/180**, 487 (1994).
64. "Selected Values of Thermodynamic Properties of Binary Alloys", eds. R. Hultgen, P. D. Desai, D. T. Hawkins, M. Gleiser, K. K. Kelley, ASM, Metals Park, Ohio, 1973.
65. A. Inoue, K. Ohtera, A. P. Tsai and T. Masumoto, Jpn. J. Appl. Phys. **27**, L479 (1988).
66. Y. He, S. J. Poon, G. J. Shiflet, Science, **241**, 1640 (1988) .
67. A. Inoue, K. Nakazato, Y. Kawamura, A. P. Tsai and T. Masumoto, Mater. Trans. JIM, **35**, 95 (1994).
68. K. Nakazato, Y. Kawamura, A. P. Tsai, A. Inoue, Appl. Phys. Lett. **63**, 2644 (1993).
69. K. Hono, Y. Zhang, A-P. Tsai, A. Inoue and T. Sakurai, Scripta Metall. Mater. **32**, 191 (1995).
70. K. Hono, Y. Zhang, A. Inoue and T. Sakurai, unpublished work.
71. T. Yogi and T. A. Nguyen, IEEE Trans. Mag. **MAG-29**, 307 (1993).
72. Y. Shiroishi, K. Yoshida, M. Futamoto and H. Aoi, J. Mag. Soc. Jpn. **17**, 784 (1993).
73. S. Iwasaki and K. Ouchi, IEEE Trans. Mag. **MAG-14**, 849 (1978) .
74. T. M. Coughlin, J. H. Judy and E. R. Wuori, IEEE Trans. Mag. **MAG-17**, 3169 (1981).
75. K. E. Johnson, J. B. Mahlke, K. J. Schulz and A. C. Wall, IEEE Trans. Mag. **MAG-29**, 215 (1993).
76. J. Zhu and H. N. Bertram, J. Appl. Phys. **63**, 3248 (1988).
77. R. D. Fisher, V. S. Au-Yeung and B. B. Sabo, IEEE Trans. Mag. **MAG-20**, 806 (1984).
78. J. W. Smits, S. B. Luitjens and F. J. A. den Broeder, J. Appl. Phys. **55**, 2260 (1984).
79. S. Iwasaki, K. Ouchi and T. Hizawa, J. Mag. Soc. Jpn. **9**, 57 (1985).
80. M. Sagoi, R. Nishikawa and T. Suzuki, IEEE Trans. Mag. **MAG-22**, 1335 (1986) .

81. K. Ouchi and S. Iwasaki, IEEE Trans. Mag. **MAG-18**, 1110 (1982) .
82. J. N. Chapman, I. R. McFadyen and J. P. C. Bernards, J. Mag. Mag. Mater. **62**, 359 (1986) .
83. A. K. Jhingan, J. Mag. Mag. Mater. **54-57**, 1685 (1986).
84. D. J. Rogers, J. N. Chapman, J. P. C. Bernards and S. B. Luitjens, IEEE Trans. Mag, **MAG-25**, 4180 (1989).
85. Y. Maeda, S. Hirono and M. Asahi, Jpn. J. Appl. Phys. **24**, L951(1985).
86. Y. Maeda, M. Asahi and M. Seki, Jpn. J. Appl. Phys. **25**, L668 (1986).
87. Y. Maeda and M. Asahi, J. Appl. Phys. **61**, 1972 (1987).
88. Y. Maeda and M. Takahashi, Jpn. J. Appl. Phys. **28**, L248 (1989).
89. K. Yoshida, H. Kakibayashi and H. Yasuoka, J. Appl. Phys. **68**, 705 (1990).
90. K. Takei and Y. Maeda, Jpn. J. Appl. Phys. **30**, L1125 (1991).
91. Y. Maeda and M. Takahashi, J. Appl. Phys. **68**, 4751 (1990).
92. J. E. Snyder and M. H. Kryder, J. Appl. Phys. **73**, 5551 (1993).
93. K. Takei, J. Suzuki, Y. Maeda and Y. Morii, IEEE Trans. Magn. **30**, 4029 (1994).
94. K. Hono, S. S. Babu, Y. Maeda, N. Hasegawa and T. Sakurai, Appl. Phys. Lett. **62**, 2504 (1993).
95. K. Hono, Y. Maeda, J-L. Li and T. Sakurai, IEEE Trans. Mag. **29**, 3745 (1993).
96. K. Hono, Y. Maeda, S. S. Babu and T. Sakurai, J. Appl. Phys. **76**, 8025 (1994).
97. K. Hono, K. Yeh, Y. Maeda and T. Sakurai, Appl. Phys. Lett. **66**, 1686 (1995).
98. J. Nishimaki, K. Hono, N. Hasegawa and T. Sakurai, Appl. Phys. Lett. **69**, 3095 (1996).
99. K. Hono, R. Okano, K. Takanashi, Y. Maeda, H. Fujimori and T. Sakurai, MRS Symposium Proceedings, Vol. 384, "Magnetic Ultrathin Films, Multilayers and Surfaces" eds. E. E. Marinero, B. Heinrich, W. F. Egelhoff, Jr., A. Fert, H.Fujimori, G. Guntherodt, R. L. White, (MRS, Pittsburgh, 1995) pp.507.
100. M. Hasebe, K. Oikawa and T. Nishizawa, J. Jpn. Inst. Metals **46**, 577 (1982).
101. R. D. Fisher, J. C. Allan and J. L. Pressesky, IEEE Trans. Mag. **MAG-22**, 352 (1986).
102. H. Tamai, K. Tagami and H. Hayashida, IEEE Trans. Mag. **MAG-24**, 2347 (1988).
103. K. Kimoto, Y. Yahisa, T. Hirano, K. Usami and S. Narishige, Jpn. J. Appl. Phys. **34**, L352 (1995).
104. M. N. Baibich, J. M. Broto, A. Fert, F. Ngyen van Dau, F. Petroff, P. Eitenne, G. Creuzet, A. Friederich and J. Chazelas, Phys. Rev. Lett. **61**, 2473 (1988).
105. S. S. P. Parkin, R. Bhadra and K. P. Roche, Phys. Rev. Lett. **66**, 2152 (1991).
106. F. Petroff, A. Barthelemy, D. H. Mosca, D. K. Lottis, A. Fert, P. A. Schroeder, W. P. Pratt, Jr., R. Loloee and S. Lequien, Phys. Rev. **B44**, 5355 (1991).
107. S. Araki, K. Yasui and Y. Narumiya, J. Phys. Soc. Jpn. **60**, 2827 (1991).
108. C. S. Santos, B. Rodmacq, M. Vaezzadeh and B. George, Appl. Phys. Lett. **59**, 126 (1991).
109. A. E. Berkowitz, J. R. Mitchell, M. J. Carely, A. P. Young, S. Zhang, F. E. Spada, F. T. Parker, A. Hutten and G. Thomas, Phys. Rev. Lett. **68**, 3745 (1992).
110. J. Q. Xiao, J. S. Jian and C. L. Chien, Phys. Rev. Lett. **68**, 3749 (1992).
111. C. L. Chien, J. Q. Xiao and J. S. Jiang, J. Appl. Phys. **73**, 5309 (1993).
112. N. Kataoka, H. Endo, K. Fukamichi and Y. Shimada, Jpn. J. Appl. Phys. **32**, 1969 (1993).
113. J. Wecker, R. von Helmolt, L. Schulz and K. Sawer, Appl. Phys. Lett. **62**, 1985 (1993).
114. H. Takeda, N. Kataoka, K. Fukamichi and Y. Shimada, Jpn. J. Appl. Phys. **33**, 102 (1994).
115. L. H. Chen, S. Jin and T. H. Tiefel, J. Mater. Res. **9**, 1134 (1994).
116. R. Okano, K. Hono, T. Takanashi, H. Fujimori and T. Sakurai, J. Appl. Phys. **77**, 5843 (1995).
117. D. E. Coates, Metall. Trans. **3**, 1203 (1972).
118. S. S. Babu, K. Hono and T. Sakurai, Appl. Sruf. Sci. **67**, 321 (1993).
119. S. S. Babu, K. Hono and T. Sakurai, Metall. Trans. A, **25A**, 499 (1994).
120. R. C. Thomson and M. K. Miller, Appl. Surf. Sci., **87/88**, 185 (1995).
121. K. Hono, A. Chiba, T. Sakurai, S. Hanada, Acta Metall.Mater. **40**, 419-425 (1992).
122. K. Hono, H. Numakura, I. A. Szabo, A. Chiba and T. Sakurai, Surf. Sci. **266**, 358-363 (1992).
123. H. Numakura, T. Yamada, M. Koiwa, I. A. Szabo, K. Hono and T. Sakurai, Defect and Diffusion Forum, **95-98**, 867 (1993).
124. A. Almazouzi, H. Numakura, M. Koiwa, K. Hono, and T. Sakurai, Intermetallics, **5**, 37 (1997).